Altered blood-brain barrier transport of nanotherapeutics in lysosomal storage diseases

Melani Solomon[1]*, Maximilian Loeck[2], Marcelle Silva-Abreu[2], Ronaldo Moscoso[1], Ronelle Bautista[1], Marco Vigo[2], and Silvia Muro[1,2,3]*

[1] Institute for Bioscience and Biotechnology Research, University of Maryland, College Park, MD, USA

[2] Institute for Bioengineering of Catalonia of the Barcelona Institute of Science and Technology, Barcelona, Spain

[3] Institute of Catalonia for Research and Advanced Studies, Barcelona, Spain

* Correspondence:
Nanocarrier targeting and transport: SM: muro@umd.edu; +34 934 020 440
Lysosomal storage disease markers: MS: melani.solomon@catalent.com

Abstract: Treatment of neurological lysosomal storage disorders (LSDs) are limited because of impermeability of the blood-brain barrier (BBB) to macromolecules. Nanoformulations targeting BBB transcytosis are being explored, but the status of these routes in LSDs is unknown. We studied nanocarriers (NCs) targeted to the transferrin receptor (TfR), ganglioside GM1 or ICAM-1, associated to the clathrin, caveolar or cell adhesion molecule (CAM) routes, respectively. We used brain endothelial cells and mouse models of acid sphingomyelinase-deficient Niemann Pick disease (NPD), and postmortem LSD patients' brains, all compared to respective controls. NC transcytosis across brain endothelial cells and brain distribution in mice were affected, yet through different mechanisms. Reduced TfR and clathrin expression were found, along with decreased transcytosis in cells and mouse brain distribution. Caveolin-1 expression and GM1 transcytosis were also reduced, yet increased GM1 levels seemed to compensate, providing similar NC brain distribution in NPD *vs.* control mice. A tendency to lower NHE-1 levels was seen, but highly increased ICAM-1 expression in cells and human brains correlated with increased transcytosis and brain distribution in mice. Thus, transcytosis-related alterations in NPD and likely other LSDs may impact therapeutic access to the brain, illustrating the need for these mechanistic studies.

Keywords: Lysosomal storage disorders, neurological diseases, blood-brain barrier, transcytosis pathways, targeted nanocarriers.

Graphical abstract:

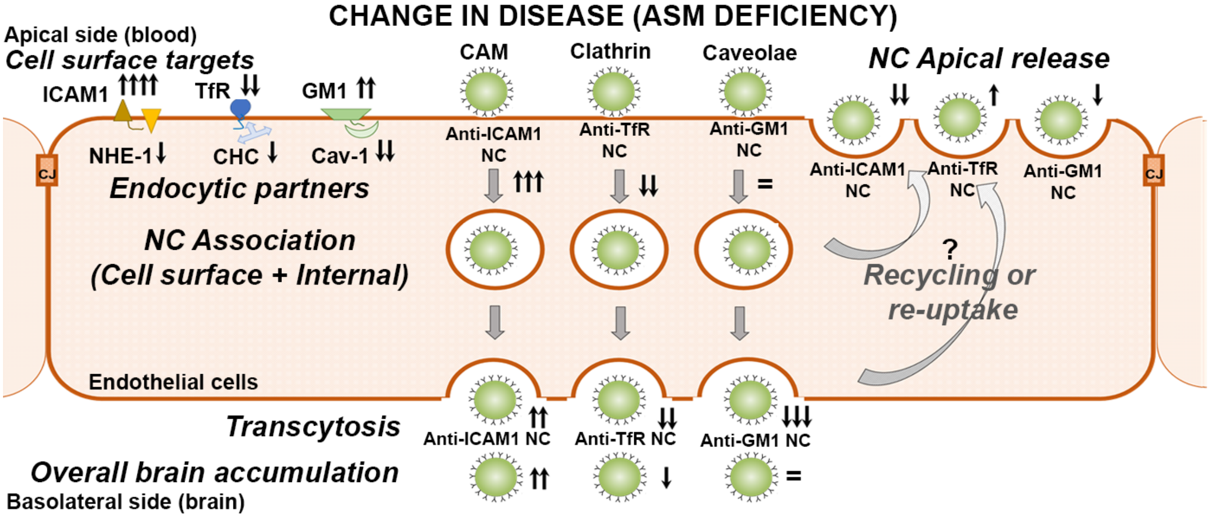

1. Introduction

Delivery of therapeutic molecules to the central nervous system is an unsurmounted challenge to this day due to the relative impermeability of the blood brain barrier (BBB) to most therapeutics [1,2]. Several strategies have been devised to overcome this limitation, including transient permeabilization of the BBB using physical and chemical approaches, administration of efflux pump inhibitors, etc. [1]. However, these strategies have found little success for delivery of macromolecular therapeutics such as enzymes and proteins [1,3]. While local delivery of macromolecular therapeutics in specific regions of the central nervous system (CNS) have been useful, the risk and complexity of such interventions is considerable, for which intravenous delivery systems would be preferred [1,3]. Transcellular transport processes across endothelial cells of the BBB can be harnessed to elicit effective delivery of therapeutic cargo into the brain parenchyma [2,3]. This group of processes, termed transcytosis, can occur from the luminal to the abluminal side of the endothelium, involving binding and uptake from the vascular side, movement through the cytoplasm in vesicles, and exocytosis at the endothelial abluminal side [2,3]. Transcytosis associates with canonical pathways such as those involving clathrin-coated pits or caveoli, or non-canonical mechanisms such as the cell adhesion molecule- (CAM) mediated pathway [3]. Cell-surface receptors and membrane elements associated with these routes can be targeted, such as the transferrin receptor (TfR), insulin receptor or LRP1 in the case of clathrin-mediated pathways, or ganglioside GM1, PV1 or aminopeptidases for caveolae-mediated processes [3-6]. The CAM pathway is induced by targeting intercellular adhesion molecule 1 (ICAM-1), a cell-surface protein overexpressed on vascular endothelial cells and cells from other tissues during inflammation [3, 7].

Drug delivery approaches to elicit macromolecular transcytosis across the BBB have mostly utilized a molecular Trojan horse strategy, where a therapeutic cargo is targeted to one of these elements using ligands or antibodies in the form of fusion proteins, conjugates or NC-mediated approaches [3-8]. Such strategies are being investigated to deliver chemotherapeutic molecules as well as agents for the treatment of Alzheimer's disease (AD), Parkinson's disease (PD), LSDs, stroke etc. [1-3]. NCs are useful tools in this regard, since they can be surface-functionalized to target these pathways, their multivalency and physicochemical parameters can be adjusted to elicit different fates, can be loaded with a variety of therapeutic cargoes or drug combinations, and can protect pharmaceuticals from the systemic environment [2,3]. NCs targeted to TfR have been shown to deliver cargo to the brain for neurodegenerative disease [6,8,9]. In some instances, the caveolar pathway has been utilized to transport therapeutics across the BBB through adsorptive mediated transcytosis [10]. The CAM pathway has been exploited using anti-ICAM1 NCs, both in cellular and mouse models [7,11].

A common drawback of exploiting vesicular transport is that cargo, particularly in the case of NCs, can get sorted to the lysosomal route instead of being exocytosed by endothelial cells into the brain parenchyma [3,11]; however this can be tuned by modulating the binding avidity of NCs to elicit transcytosis [9,11]. Yet, such approaches still remain suboptimal, thus requiring high doses and multiple administrations to achieve a meaningful therapeutic effect [1,3]. Hence, a deeper understanding of transcytosis mechanisms is required for clinical translation of therapeutics for brain delivery.

An important factor that is often overlooked in the design of these therapeutic strategies is that the particular neuropathology to be treated can involve the BBB and, thus, alter its ability to transport therapeutics into the brain [3]. In several neurological diseases, a disruption of normal BBB function has been observed, involving inflammation and further worsening pathological outcomes [12-14]. Additionally, some neurological diseases are accompanied by disturbances affecting vesicular trafficking [13-22]. These trafficking alterations could affect transport of therapeutic cargo through the endothelium into the brain parenchyma. In fact, several studies have shown altered uptake of ligands and NCs through different pathways in different *in vitro, ex vivo* and *in vivo* models for neurological diseases such as AD [14], PD [15], lysosomal storage diseases [13,16-22], as well as cancers [23].

An important feature of these diseases is that they involve abnormal cellular storage of substances, generally due to a dysfunction in the endo-lysosomal and autophagic pathways [12,13,17,21,24], even when the accumulated substance is a secondary consequence to a primary genetic alteration that does not directly affect the associated metabolic pathway [25]. Such dysfunctions can lead to cytoplasmic crowding due to the accumulation of vesicles, which can affect organelle transport [26]. Hence, an important question is the impact of such lysosomal storage on transcytosis across brain endothelial cells in these diseases.

To understand this impact in the context of delivering therapeutic NC to the brain, this study utilized models of an LSD caused by acid sphingomyelinase (ASM) deficiency, known as Niemann Pick disease (NPD) [27]. ASM deficiency leads to accumulation of sphingomyelin and cholesterol in the lysosomes of cells [27]. Although enzyme replacement therapy (ERT) is successful in restoring the peripheral manifestations of this disorder it is not effective, and thus not prescribed for the progressive neurological form due to the impermeability of the BBB to enzymes, leading to mortality in early childhood [27]. Using the ASM knock-out (ASM KO) mouse model for NPD, pharmacological models inhibiting ASM in endothelial cells, and postmortem brain samples from patients with LSDs, this study evaluated the factors that affect transcytosis via clathrin, caveolar or CAM pathways, of targeted NCs in a pathological BBB.

2. Materials and Methods

Antibodies and Reagents. Antibodies recognized the following proteins: human clathrin heavy chain (Abcam, Cambridge, United Kingdom), caveolin-1 (ThermoFisher Scientific, Waltham, MA) or human (clone R6.5) or murine (clone YN1) ICAM-1 (American Type Culture Collection, Manassas, VA), human (clone T56/14; EMD Millipore, Billerica, MA) or mouse (clone 8D3; Novus Biologicals, Littleton CO) transferrin receptor, ganglioside GM1 (Bioss Antibodies, Woburn, MA), human GAPDH (Santa Cruz Biotechnology, Dallas, TX), or human sodium/proton NHE-1 (BD Biosciences, Franklin Lakes, NJ). Other antibodies included murine, rat and rabbit IgG (Jackson Immunoresearch, West Grove, PA), fluorescent secondary antibodies (Life Technologies, Carlsbad, CA) and HRP-conjugated antibodies (GE Healthcare Bio-Sciences, Pittsburgh, PA). AF594-labeled Cholera-toxin B (CTB) was from Thermofisher Scientific (Waltham, MA). Fluoresbrite® polystyrene beads (100 nm diameter) were from Polysciences Inc. (Warrington, PA). Iodine was from Perkin Elmer (Billerica, MA), Iodogen was from Thermofisher Scientific (Waltham, MA) and Bio-Spin® P-6 Gel Columns were from Biorad (Hercules, CA). One μm pore size Transwell filters and cell cultureware were obtained from Thermofisher Scientific (Waltham, MA). Cell culture media and supplements were from Cellgro (Manassas, VA), Gibco BRL (Grand Island, NY) and EMD Millipore Corporation (Billerica, MA). Poly(lactic-co-glycolic acid) or PLGA (50:50 copolymer ratio; 31,000 mean MW), and all other reagents were from Sigma Aldrich (St. Louis, MO), unless otherwise noted.

Cell Cultures. Human brain microvascular endothelial cells (HBMECs) from Cell Systems (Kirkland, WA) were grown at 37 °C, 5% CO_2, and 95% humidity in RPMI medium supplemented with 20% fetal bovine serum (FBS), 2 mM L-glutamine, 30 μg/mL endothelial cell growth supplement, 100 μg/mL heparin, 100 units/mL penicillin and 100 μg/mL streptomycin. Cells were grown on gelatin-coated coverslips for immunofluorescence, in 6-well plates for Western blotting, in T25 flasks for flow cytometry, or on the apical side of 1 μm pore-size transwell filters (ThermoFisher Scientific, Waltham, MA). Where indicated, cells were treated with 20 μM imipramine for 48 h to induce acid sphingomyelinase deficiency and 10 ng/mL tumor necrosis factor-α (TNFα) overnight to simulate inflammation, both occurring in NPD [27]. For simplicity, they are termed diseased cells thereafter.

Human Brain samples. Frozen post-mortem brain samples from the cerebral cortex of three control non-LSD patients and ten LSD patients were obtained from the NIH Blood and Tissue Bank maintained at the University of Maryland (see Supplementary Table S1 for details). These samples contained no patient identifiable information and thus, required no human subjects regulation.

Western blotting. Brain samples (50 mg pieces) and HBMECs were lysed, homogenized and sonicated on ice, then centrifuged at 16000 g for 20 min at 4 °C to collect supernatants. Proteins in the cell lysate were separated by SDS-PAGE, transferred to a PVDF membrane, and ICAM1, clathrin heavy chain (CHC), sodium/proton exchanger NHE-1 or caveolin-1 (Cav-1) were probed by Western blotting. The intensity of the protein bands was determined by densitometry using the Gel analyzer tool in ImageJ (National Institutes of Health, Bethesda, MD) and normalized to housekeeping GAPDH or β-actin control to calculate Test protein/Housekeeping protein ratio.

Immunostaining of brain tissues and cells. Human brain samples were embedded in Paraplast wax and the resulting blocks were sectioned (15 μm thickness) with a HM 430 Sliding Microtome (ThermoFisher Scientific, Waltham, MA). Sections were deparaffinized, immersed in antigen retrieval buffer (10 mM sodium citrate, 0.05% Tween 20, pH 6.0) and microwaved at 800 W power for 10 min. Sections were permeabilized and treated with the respective primary antibodies (anti-Cav-1, anti-CHC or anti-ICAM1), followed by fluorescently labeled secondary antibodies in a humidifying chamber, then incubated with DAPI and mounted with Mowiol. Mouse brains were freshly harvested, embedded in Tissue-tek cryo OCT compound (Sakura Finetek, Torrance, CA) and frozen to -80 °C. Then, samples were cryosectioned using a rotary microtome (Model 855 Histostat–cryostat, Buffalo NY), collected onto positively charged glass slides, treated with AF594-labeled CTB in a humidified chamber, stained with DAPI and mounted with Mowiol. Regarding cells, they were fixed with 2% paraformaldehyde (PFA) and incubated with the anti-ICAM1 and Alexa-Fluor555-labeled secondary antibody, then incubated with DAPI and mounted with Mowiol.

All samples were imaged using an Olympus IX81 fluorescence microscope (Olympus, Center Valley, PA) and a 60X PlanApo objective. Images were acquired using Orca-ER camera (Hamamatsu, Bridgewater, NJ) and the fluorescence signal was analyzed with ImagePro 6.3 (Media Cybernetics, Silver Spring, MD). The number of nuclei were used to normalize Fluorescence Intensity of any given marker in brain sections.

Flow cytometry. Control *vs.* diseased HBMECs were trypsinized, fixed, and incubated with anti-ICAM1, anti-GM1, or anti-TfR at 4 ºC for 1 h, then centrifuged, washed and incubated with fluorophore-conjugated secondary antibodies. Cells were centrifuged, washed, suspended in PBS and analyzed by flow cytometry analysis using BD FACS Caliber (Olympus, Center Valley, PA). Forward and side scatter data from 10,000 events were acquired and analyzed by FlowJo software (BD life sciences, USA). Relative expression of the indicated markers was calculated as follows:

$$\boldsymbol{Relative\ expression} = \frac{\boldsymbol{Receptor\ signal\ (specific\ antibody)}}{\boldsymbol{Background\ signal\ (non\ specific\ IgG)}}$$

where, $\textit{Signal} = \textit{Expression intensity x Expressing fraction of the cell population}$

Radioactive labeling of antibodies. Antibodies were labeled with Iodine-125 (^{125}I), as described [11, 28, 29]. Briefly, 100 µg of each antibody was reacted with 20 µCi of Na^{125}I at room temperature for 5 min in the presence of Iodogen reagent, followed by centrifugation in gel filtration columns to remove free ^{125}I. The amount of radiolabeled antibody (counts per minute, CPM) was determined using a gamma counter (Wizard2, Perkin Elmer, Billerica, MA), and respective protein concentration was determined using a Bradford assay (Biorad, Hercules, CA), to calculate the specific activity of ^{125}I-antibody as published [11, 28, 29], according to the following equation:

$$\boldsymbol{Specific\ activity\ \left(\frac{CPM}{\mu g}\right) = \frac{Radioactive\ counts\ in\ protein\ (\frac{CPM}{ml})}{Protein\ concentration\ (\frac{\mu g}{mL})}}$$

NC preparation. PLGA NCs were prepared by nanoprecipitation and solvent evaporation, as in our previous publications [30-32]. Both PLGA and commercial polystyrene formulations were coated by adsorption using established protocols [11, 31], with either non-specific IgG, anti-ICAM1, anti-TfR or anti-GM1 antibodies. At the used concentrations, adsorption has been shown to favor outward display of antibodies [33]. Briefly, 7,000 µg/mL NCs and 1.5 µM total protein were incubated for 1 h at room temperature for polystyrene NCs or for 16 h at 4 ^{o}C for PLGA NCs, then diluted in PBS and centrifuged at 12,000 rpm for 3 min to remove non-coated proteins, and pellets were finally re-suspended in 0.3-1% BSA in PBS and sonicated. NCs were characterized (see Table 1) in terms of hydrodynamic diameter, polydispersity index (PDI), and ζ-potential by dynamic light scattering (DLS; Zetasizer Nano-ZS90, Malvern Instruments; Westborough, MA). The number of antibody molecules per NC was determined by using radiolabeled antibodies and determining the radioactive content associated with NC pellets, as described [11, 31], using the following equation:

$$\boldsymbol{Antibody\ \left(\frac{molecules}{NC}\right) = \frac{CPM\ pellet\ \times N}{Specific\ acitvity\ \left(\frac{CPM}{\mu g}\right) \times MW\ \times Number\ of\ NCs}}$$

Where, N = Avogadro's number = 6.023 x 10^{23} and MW = 150,000 Da for an IgG molecule.

NC binding and blocking. Control *vs.* diseased HBMECs were incubated at 37 ^{o}C for 30 min or 1 h with non-labeled PLGA NCs or green-fluorescent polystyrene NCs, both coated with either non-specific IgG, anti-TfR, anti-GM1 or anti-ICAM1 as described in the respective figures. For blocking experiments, 3.5 µg/ml free anti-ICAM1, anti-TfR, or anti-GM1 were added to wells 15 min prior to incubation with respective NCs and then maintained during their 1 h NC incubation with cells. Short incubation times were preferred to determine binding to avoid confusing results derived from NCs intracellular trafficking, recycling, receptor secretion of intracellular pools, etc. Cells were then washed and fixed with 2% PFA. For non-labeled PLGA NCs, cells were permeabilized with 0.1% Triton X-100 and stained with green-fluorescent secondary antibodies to visualize antibody-coated NCs. Samples were analyzed by fluorescence microscopy, as described above, and an algorithm was used to quantify the number of objects per cell whose green fluorescence had the minimal size of NCs and surpassed background fluorescence [11].

NC uptake specificity and antibody coat colocalization. TNFα-activated HBMECs were incubated at 37 °C for 30 min or 1 h, as indicated, with green-fluorescent polystyrene NCs coated with either non-specific IgG, anti-TfR, anti-GM1 or anti-ICAM1 in the presence *vs*. absence of 3 mM amiloride, 50 μM monodansylcadaverine, or 1 μg/ml filipin. Non-bound NCs were removed by washing cells and surface bound NCs were counterstained with secondary antibody labeled in a second color. Cells were then permeabilized and both surface + internal NCs were stained with secondary antibody labeled in a third color. Following this protocol surface located NCs are labeled in three colors *vs* internalized NCs, which are labeled in two colors, from which internalization and antibody-coat colocalization can be quantified as described [11, 19, 20].

NC transcytosis and apical release. PLGA NCs coated with ^{125}I-IgG, ^{125}I-anti-TfR, ^{125}I-anti-GM1 or ^{125}I-anti-ICAM1 were added to the apical chamber at a dose of 6-8 x 10^9 to NC/well above HBMEC monolayers (control *vs*. diseased) grown on transwells and incubated at 37 °C for a 30 min binding pulse. As an additional control, free antibody (^{125}I-anti-ICAM1) was similarly tested at a dose of 10 μg/mL. NCs or antibody were removed by wash from the apical and basolateral chambers and cells were incubated in NC-free medium to enable transcytosis of pre-bound NCs. Then, the basolateral or apical fractions were collected at various time points from 2-24 h and the radioisotope content was measured using a gamma counter (Wizard2, Perkin Elmer, Billerica, MA) to calculate the number of NCs. Free ^{125}I was separated and quantified as described [7, 11, 28], to correct for this factor in case free ^{125}I were produced by degradation during experiments. Briefly, TCA was added to each fraction for 15 min to precipitate proteins followed by centrifugation at 3500 rpm for 5 min to separate free ^{125}I in the supernatant, which was then subtracted from total CPM values. These data were used to calculate the number of NCs in each fraction and the apparent permeability coefficient (Papp) as follows:

$$\boldsymbol{NC\ fraction = \frac{CPM\ fraction\ x\ NC\ dose}{CPM\ dose}}$$

$$\boldsymbol{Papp\ (cm/s) = \frac{(CPM\ basolateral\ x\ Vol.)}{(A\ x\ t\ x\ CPM\ dose)}}$$

where, CPM are the corrected ^{125}I counts-per-minute in each respective chamber ($CPM_{fraction}$), NCs_{dose} are the number of NCs initially added to the apical chamber, A is the surface area of the filter membrane (cm^2), Vol. is volume of medium in the apical chamber (mL), and t is time of incubation (s), as described [7, 11, 28].

Similarly, μg of antibody in the fraction was calculated as follows:

$$\boldsymbol{Antibody\ fraction\ (\mu g) = \frac{CPM\ fraction\ x\ Antibody\ dose\ (\mu m)}{CPM\ dose}}$$

Dextran transport control. HBMECs monolayers grown on transwells were incubated for 30 min at 37 °C with 0.5 mg/mL Texas Red-labeled dextran added to the apical chamber above the cells. Then, apical and basolateral fractions were collected and their dextran content was determined using SYNERGY HTX microplate reader (Agilent BioTek, Santa Clara, CA, USA).

***In vivo* biodistribution of NCs**. C57BL/6 mice, either wildtype control or ASM KO, were anesthetized and intravenously (*i.v.*) injected at 1.8 x 10^{13} NCs/kg body weight with either IgG NCs, anti-TfR NCs, anti-GM1 NCs or anti-ICAM1 NCs (polystyrene or PLGA). As in our previous studies [11, 30, 31, 34], all formulations were coated with tracer amounts (5%) of non-specific ^{125}I-IgG along with the targeting antibody to ensure coated NCs, not free antibody, are tracked by comparison among different formulations: *i.e.* if ^{125}I-IgG would detach from NCs, all formulations would show similar results and would be similar to free ^{125}I-IgG, also injected as a control. Blood samples were collected from the retro-orbital sinus at 2, 15, and 30 min after injection, and target (brain) or clearance (liver) organs were collected at sacrifice (30 min). The radioactive content and weight of the samples were determined to calculate, as described [11, 31, 32], the percentage injected dose (%ID), %ID per gram of organ (%ID/g; for organ concentration), Localization ratio (LR; a tissue-to-blood measurement) and specificity index (SI; targeted to non-targeted comparison), using the following equations:

$$\boldsymbol{Localization\ ratio, LR} = \frac{\boldsymbol{\%\,ID/g\ organ}}{\boldsymbol{\%\,ID/g\ blood}}$$

$$\boldsymbol{Specificity\ index, SI} = \frac{\boldsymbol{\%ID\ of\ targeted\ NC}}{\boldsymbol{\%ID\ of\ nonspecific\ NC}}$$

$$\boldsymbol{Targeting\ to\ clearance\ ratio} = \frac{\boldsymbol{SI\ (Brain)}}{\boldsymbol{SI\ (Liver)}}$$

All animal experiments were performed in accordance with IACUC and University of Maryland regulations and the Guide for the Care and Use of Laboratory Animals of the U.S National Institutes of Health.

Statistics. Data are represented as the mean ± standard error of the mean (SEM). Microscopy included 2-3 independent wells per 2-3 independent experiments, not analyzed in bulk but cell-by-cell for a minimum of 20 randomly selected cells per coverslip or transwell. Transcytosis encompassed 4 transwells per ≥ 3 independent experiments. Flow cytometry involved n ≥ 3 runs per ≥ 2 independent experiments. Western blotting encompassed n ≥ 3 runs from independent cell lysates and n ≥ 6 runs from n ≥ 3 independent brain tissue lysates. Immunostainings were performed on n ≥ 3 independent samples. For *in vivo* experiments, n ≥ 5 mice were used per condition. Multiple groups were compared by one-way ANOVA and a Holm-Sidak post-hoc test. For two-group comparisons, student's *t*-test was used. Significance was determined assuming a p level of 0.05.

3. Results

3.1. Altered *in vivo* brain biodistribution of targeted NCs in NPD mice. Since changes in transport of NCs across the BBB would alter NC biodistribution to the brain, this was first evaluated *in vivo*. For these experiments we preferred non-degradable polystyrene NC models over biodegradable PLGA NCs to avoid the potential contribution of NC degradation to biodistribution data, which would confound our interpretation of trafficking processes. Demonstrating the validity of this model, polystyrene NCs had similar physicochemical properties and biodistribution as PLGA NCs, as in our previous studies [30-32, 35]. For instance, PLGA NCs coated with non-specific antibody (IgG) or antibodies targeting clathrin (anti-TfR), caveolar (anti-GM1) or CAM (anti-ICAM1) pathways had mean diameter between 207-223.8 nm, PDI between 0.139-0.165 and ζ-potential between -22.0 to -26.1 mV, while respective polystyrene formulations ranged between 196-219.9 nm, 0.120-0.137 PDI and -23.5 to -26.4 mV (Table 1). The number of antibody molecules per NC was also relatively similar, between 177-244 for PLGA formulations and 177-233 for polystyrene models (Table 1). These formulations are relatively stable, including minimal protein detachment (<20%) after incubation for 72 h at 37 °C in 50% serum [36]. They also endure minimal changes in polydispersity or hydrodynamic diameter (5-20%) when stored for two weeks at 4 °C or after incubation in 50% serum for 48 h at 37 °C, can be lyophilized and reconstituted without affecting these parameters, and show spherical shape by electron microscopy [11, 31, 32, 36]. As an additional validation, anti-ICAM1 polystyrene NCs had similar circulation as PLGA counterparts (*e.g.* 7.3 and 7.6 %ID in blood 30 min after *i.v.* injection in wildtype mice; Supplementary Table S2) and similar liver (40 and 34 %ID/g), lung (104 and 114 %ID/g) and brain distribution (0.2 and 0.2 %ID/g). It is worth noticing that neurological LSDs affect not only the CNS but also visceral organs [3, 16, 27] and, thus, this broad NC distribution is ideal for treatment.

Table 1. Characterization of NC formulations

Formulation	Size (nm)		PDI		ζ-potential (mV)		Antibody molecules/NC	
	Mean	SEM	Mean	SEM	Mean	SEM	Mean	SEM
PLGA								
Non-coated	164.6	12.3	0.080	0.010	-39.9	0.6	--	--
IgG	207.0	8.5	0.139	0.047	-24.2	0.3	183	24
Anti-TfR	211.4	3.6	0.151	0.069	-26.1	0.2	201	8
Anti-GM1	213.0	5.4	0.157	0.061	-25.4	0.5	177	35
Anti-ICAM1	223.8	4.4	0.165	0.060	-22.0	0.7	244	15
Polystyrene								
Non-coated	127.3	2.0	0.070	0.020	-44.9	9.0	--	--
IgG	219.9	7.8	0.137	0.050	-23.5	0.6	177	5
Anti-TfR	196.0	6.6	0.132	0.053	-25.1	3.3	180	2
Anti-GM1	197.4	7.9	0.126	0.073	-26.4	2.2	233	6
Anti-ICAM1	217.0	3.3	0.120	0.027	-24.9	0.3	223	3

PDI: Polydispersity Index; SEM = Standard error of the mean

It must be noted that, as in our previous publications [11, 31, 35, 36], all *in vivo* tests in this study involved NCs coated with tracer amounts of ^{125}I-IgG along with non-labeled targeting antibody. Thus, if antibodies would detach from the NC, the tracer would behave as free ^{125}I-IgG injected alone and we would observe no difference between NCs targeted to different receptors or control IgG NCs. Validating this, ^{125}I-IgG on anti-ICAM NCs showed a different biodistribution compared to NCs coated with ^{125}I-IgG alone or free ^{125}I-IgG (Supplementary Figure S1): *e.g.* both NCs exhibited faster clearance from circulation (4.5 %ID and 6.4 %ID *vs.* 65.7 %ID, respectively, at 30 min; Supplementary Figure S1A) and only ^{125}I-

IgG on anti-ICAM1 NCs targeted the lungs (154.8 %ID/g *vs.* 9.4 %ID/g and 7.7 %ID/g; Supplementary Figure S1B).

Next, we sought to compare the biodistribution of validated, model polystyrene formulations targeted to different pathways in wildtype *vs.* ASM KO mice. The ASM KO mouse is the animal model for NPD and exhibits neurological deficits similar to that of patients [27, 37]. Previous ERT studies using this model showed no recovery in neurological function after *i.v.* injections with recombinant ASM [37], while intracerebroventricular injections showed partial recovery [38]. Hence, this is a suitable model to investigate whether NCs hold potential to improve brain targeting from the systemic route.

Following *i.v.* injection in wildtype mice, anti-ICAM1 NCs cleared much faster from the circulation compared to anti-GM1 NCs and anti-TfR NCs (*e.g.* 12, 32, and 56 %ID, respectively, after 2 min), though all formulations reached values below 18 %ID by 30 min (Figure 1A). All NCs accumulated to a similar extent in the liver (30-36 %ID/g; Supplementary Figure S2A), yet anti-TfR NCs and anti-GM1 NCs preferentially distributed to the spleen (154 and 70 %ID/g), while anti-ICAM1 NCs preferentially accumulated in the lungs (155 %ID/g; Supplementary Figure S2A), as in previous studies [30-32, 35]. As for the brain, all formulations increased brain distribution compared to control IgG NCs, *i.e.* 2-, 2-, and 1.5-fold for anti-TfR NCs, anti-GM1 NCs, and anti-ICAM1 NCs, respectively (Supplementary Figure S2B). However, this fraction also included NCs in the brain circulation and different formulations had different levels in circulation (Figure 1A). Hence, the %ID/g in this organ was normalized by the %ID/g in blood for a more reliable tissue-to-blood parameter, termed localization ratio (LR; see Materials and Methods). Based on LR, anti-ICAM1 NCs exhibited slightly higher (1.5- and 2.3-fold increase) brain accumulation in compared to anti-TfR NCs and anti-GM1 NCs, respectively (Figure 1B).

These formulations were then injected in ASM KO mice to study their biodistribution. Anti-ICAM1 NCs displayed a 2-fold increased accumulation in the brain of ASM KO mice compared to control mice, surpassing by 3-3.5 fold the other formulations (Figure 1B). To ensure brain biodistribution changes were due to specific processes, such as targeted BBB transport, we first calculated the specificity index (SI) in the brain, *i.e.* LR in the brain of mice injected with targeted NCs divided by LR in the brain of mice injected with control IgG NCs. Then, we normalized the SI in the brain to that of the liver to extract brain specific changes (Figure 1C; see Materials and Methods). This parameter showed a brain-specific decrease for anti-TfR NCs in ASM KO mice (≈ 35%), no change for anti-GM1 NCs, and ≈ 3-fold increase for anti-ICAM1 NCs (Figure 1C).

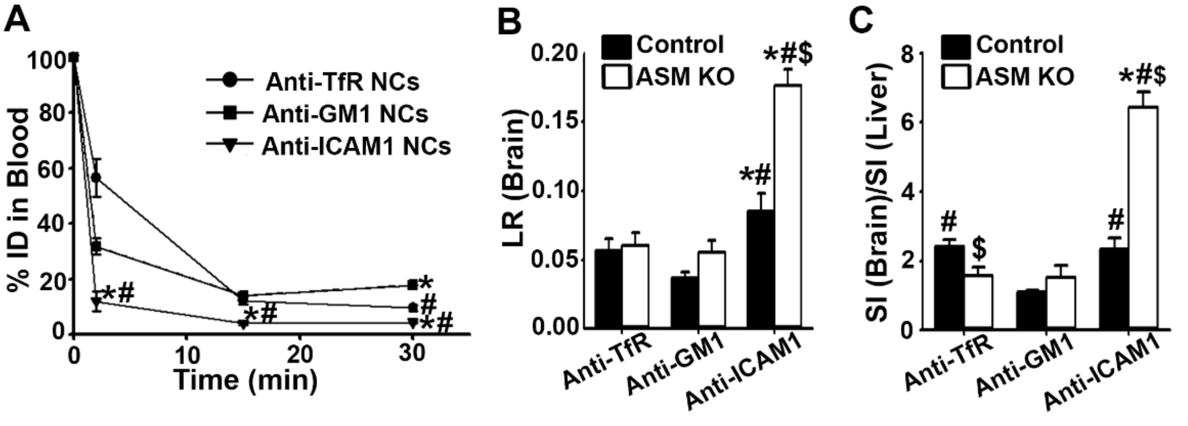

Figure 1: Biodistribution of targeted NCs in control and ASM KO mice. (A) Circulation at the indicated times and (B, C) brain biodistribution 30 min after *i.v.* injection in wildtype (Control) or ASM KO mice of model polystyrene NCs coated with tracer amounts of ^{125}I-IgG along with anti-TfR, anti-GM1 or anti-ICAM1. Weight and ^{125}I

content were determined after sacrifice to calculate: (A) the percentage of the injected dose (%ID) in the circulation of control mice, (B) the localization ratio (LR) calculated as %ID/g in brain : %ID/g in blood, and (C) the specificity index (SI) of the brain (brain LR for targeted NCs : brain LR for non-targeted IgG NCs) normalized to the SI of the liver (liver LR for targeted NCs : liver LR for non-targeted IgG NCs). Data are Mean ± SEM. *Compared to anti-TfR NCs, #compared to anti-GM1 NCs, $^{\$}$compared to control mice ($p < 0.05$ by Student's t test).

3.2. Model validations and altered NC targeting to NPD brain endothelial cells. Guided by previous results, the ability of these NCs to target brain endothelial cells, the first step preceding BBB transcytosis, was investigated. As for *in vivo* assays, the targeting specificity of antibody-coated NCs was first verified in human brain microvascular endothelial cells (HBMECs) compared to control IgG NCs, resulting in 15-, 3-, and 60-fold higher cellular association of anti-TfR NCs, anti-GM1 NCs and anti-ICAM1 NCs respectively (not shown). Also, cells were co-incubated with antibody-coated NCs in the presence *vs.* absence of free antibody to block respective targets. This reduced binding of anti-TfR NCs, anti-GM1 NCs, and anti-ICAM1 NCs by 95%, 85% and 95%, respectively (Supplementary Figure S3). Cell uptake was additionally compared in the presence *vs.* absence of inhibitors of the clathrin (MDC), caveolar (filipin), and CAM (amiloride) pathways, previously validated using respective ligands [20]. Uptake of anti-TfR NCs, anti-GM1 NCs, and anti-ICAM1 NCs was reduced by 80 %, 75% and 43%, respectively (Supplementary Figure S4).

Thereafter, we studied NCs in a disease model. Since no brain endothelial cell lines from NPD patients or ASM KO mice are available, we used HBMECs treated with imipramine to pharmacologically induce ASM deficiency [39] and TNFα to simulate an inflammatory phenotype typical in NPD [27] and many other LSDs [16]. Imipramine treated cells accumulated ≈ 7-fold increased levels of ASM substrate, sphingomyelin, validating this NPD model (Supplementary Figure S5). Also, since cell culture represents simpler and more controlled models than mice, we opted to use biodegradable PLGA NCs, whose physicochemical properties and biodistribution were similar to polystyrene models (see Table 1 and Supplementary Table S2) and are more translationally relevant. PLGA NCs targeted to each of the three pathways behaved similarly to polystyrene NCs, both in control and disease (Supplementary Figure S6).

Importantly, fluorescence microscopy data on cells growing on coverslips, to avoid transcytosis and focus on binding first, indicated that accumulation of anti-TfR NCs in brain endothelial cells modeling NPD decreased by 75% compared to control cells, that of anti-GM1 NCs remained unchanged, and that of anti-ICAM1 NCs increased by 20-fold (Figure 2A), a similar trend to that observed *in vivo* (Figure 1C). Additionally, data obtained from cells grown on transwells, where transcytosis is possible [7, 11], showed lack of change for anti-GM1 NCs and 5-fold increased accumulation for anti-ICAM1 in NPD *vs.* control conditions (Figure 2B), similar to findings from cells grown on coverslips (Figure 2A). Yet, surprisingly, we observed a 1.4-fold increased accumulation for anti-TfR NCs (Figure 2B), opposite to the coverslip model, which was also similar for polystyrene NCs and PLGA NCs (Supplementary Figure S6).

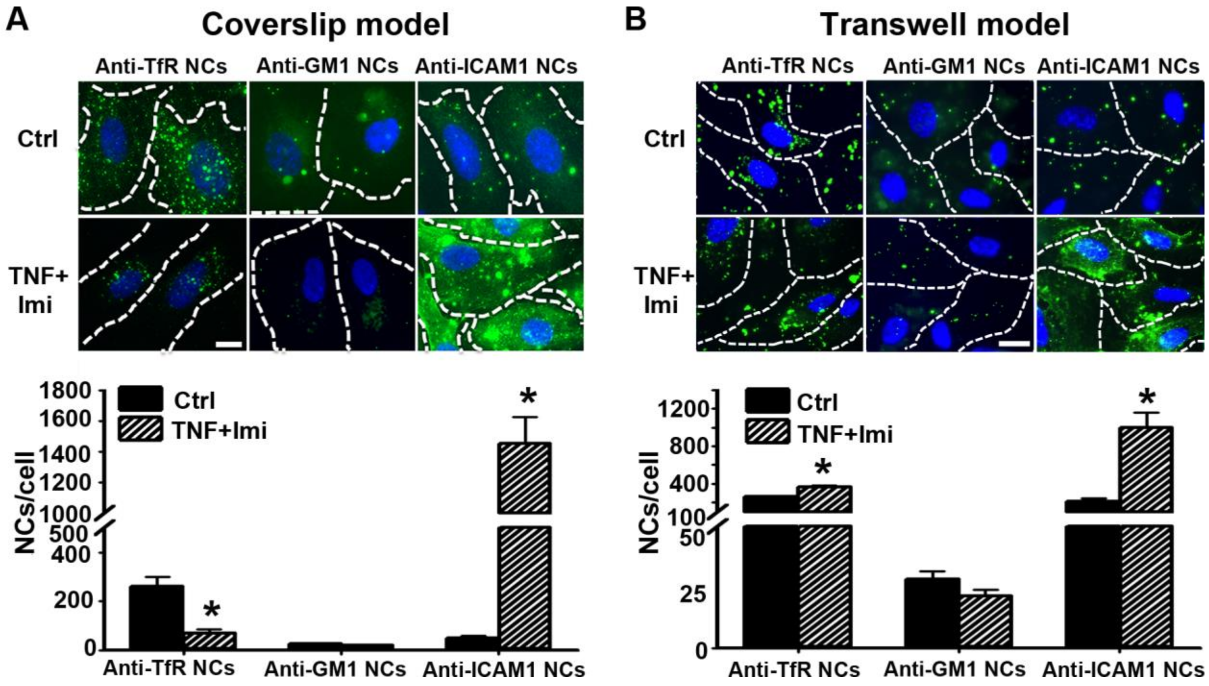

Figure 2: Targeting of NCs to control and NPD brain endothelial cell models. Immunofluorescence micrographs (top panels) and quantification (bottom panels), showing interaction of PLGA NCs coated with anti-TfR, anti-GM1 or anti-ICAM1 with HBMECs grown on (A) coverslips or (B) Transwells, either untreated (Ctrl) or treated with 20 μM imipramine + 10 ng/ml TNFα (TNF+Imi) to mimic NPD. NC incubations were conducted for 30 min at 37 °C, after which cells were fixed, permeabilized, and incubated with respective FITC-labeled secondary antibodies (green) to detect antibody-coated NCs and DAPI (blue) to stain cell nuclei. Scale bar = 10 μm. Data expressed as mean ± SEM. *Comparison with control cells ($p<0.05$ by Student's t-test).

Different results for anti-TfR NCs in coverslips *vs*. transwell models may associate to the fact that only the latter model represents an endothelial barrier separating apical and basolateral compartments, where transcytosis is possible. Verifying this, we observed that in transwells, HBMECs' associated TEER increased over time and was not altered by treating cells to mimic the disease status (Figure 3A). Also, confluent monolayers presented VE-cadherin at the cell-cell junctions (Figure 3B) and dextran, antibody, or antibody-coated NCs did not freely diffuse to the basolateral chamber (Figure 3C). This restriction was not merely due to non-specific interaction of NCs with the transwell filter (Supplementary Figure S7). For instance, while antibody-coated NCs did not leak trough the cell monolayer, they traversed the pores of cell-free transwells (Supplementary Figure S7A) and the amount of NCs at the basolateral side surpassed by 75-fold those found in the filter, demonstrating that non-specific retention in filters or clogging of pores are not limiting factors (Supplementary Figure S7B). The amount of NCs that crossed the cell monolayer were within the range of those found in said monolayer, as expected for transcytosis of NCs that interacted with cell receptors and get transported by cells (Supplementary Figure S7B).

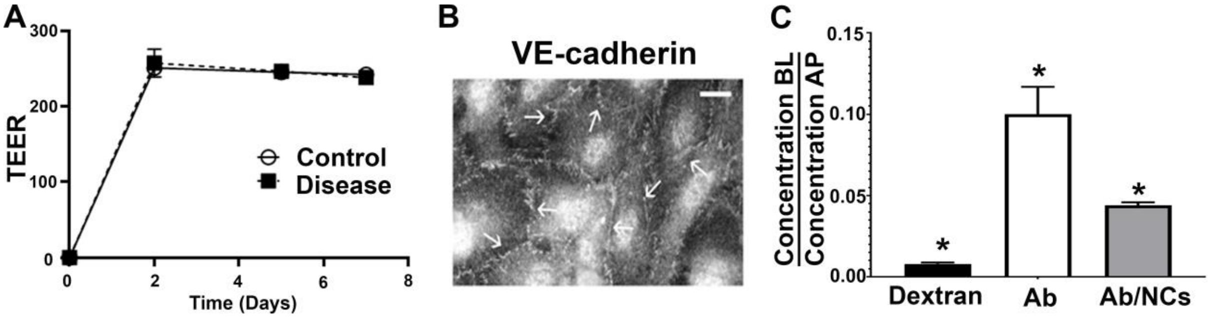

Figure 3: Brain endothelial cell barrier model. (A) TEER measurements of HBMECs grown on transwell filters over a period of 7 days, either as untreated (Control) or treated with 20 μM imipramine on day 5 (Disease). (B) Confluent HBMECs stained for VE-cadherin (arrows). Scale bar = 10 μm. (C) HBMECs were incubated for 30 min at 37 °C with Texas Red dextran, ^{125}I-labeled anti-ICAM1 antibody alone or ^{125}I-labeled anti-ICAM1 PLGA NCs added to the apical chamber, after which both the apical and basolateral cell medium were collected. For dextran, fluorescence measurements were determined using a plate reader while for the antibody and antibody-coated NC, ^{125}I content was determined to calculate respective NC concentrations in both chambers to assess barrier function. Data expressed as mean ± SEM. *Comparison with the apical chamber ($p<0.05$ by Student's t-test).

After this barrier verification, we examined transcytosis using NCs coated with ^{125}I-labeled antibody. To enable precise quantification of minute amounts, all ^{125}I-antibody was specific instead of mixing specific antibody with ^{125}I-IgG tracer, used for *in vivo* studies. This protocol tracks NCs coated with antibodies, not free or detached antibodies, since ^{125}I-anti-ICAM1 NCs were 60-fold specific over ^{125}I-IgG NCs (not shown), while NCs coated with a mixture of ^{125}I-anti-ICAM1+IgG had similar cell interaction and transcytosis than NCs coated with anti-ICAM1+^{125}I-IgG [11]. Also, the immunofluorescence pattern of free anti-ICAM1 bound to cells was different (diffuse and spread; Figure 4A) compared to NC-coated anti-ICAM1 (punctate; Figure 4B), where 99% cell-bound NCs had anti-ICAM1 and 92% of the NCs had anti-ICAM1 even after 58% cell internalization had been observed (Figure 4C). Additionally, anti-ICAM1 NCs found in the basolateral chamber after transcytosis had similar size to those originally added to the apical chamber, and they were larger than NCs without an antibody coat (Figure 4D), as expected.

Taken together, these data indicate that our endothelial cell barrier model could be used to study transport of antibody coated NCs in control and disease conditions.

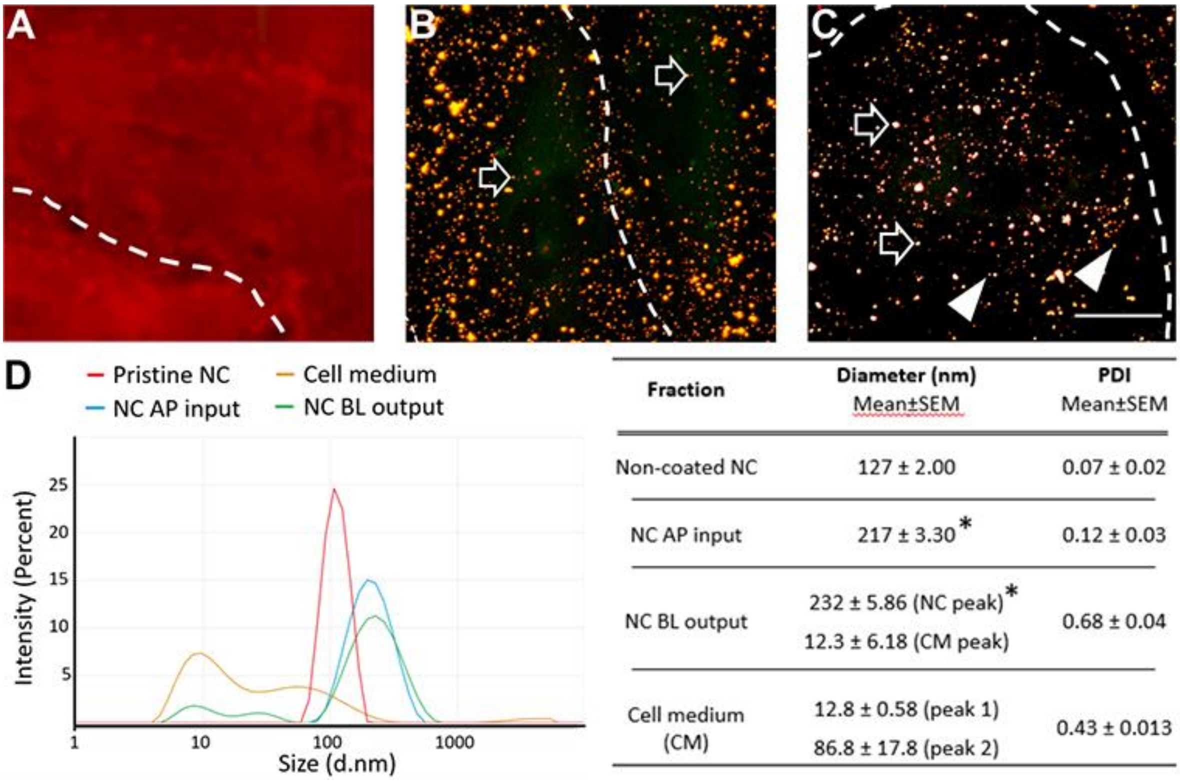

Fraction	Diameter (nm) Mean±SEM	PDI Mean±SEM
Non-coated NC	127 ± 2.00	0.07 ± 0.02
NC AP input	217 ± 3.30*	0.12 ± 0.03
NC BL output	232 ± 5.86 (NC peak)* 12.3 ± 6.18 (CM peak)	0.68 ± 0.04
Cell medium (CM)	12.8 ± 0.58 (peak 1) 86.8 ± 17.8 (peak 2)	0.43 ± 0.013

Figure 4. NCs maintain their antibody coat during binding, uptake, and transcytosis across brain endothelial cells. (A) Fluorescence microscopy of TNF-treated HBMECs incubated for 30 min with anti-ICAM1 followed by red-AlexaFluo555 secondary antibody. (B) Fluorescence microscopy of TNFα-activated HBMECs incubated for 30 min with green-fluorescent polystyrene NCs coated with anti-ICAM1 followed by red-AlexaFluor555 secondary antibody. (A,B) Fixed cells to allow cell-surface binding without uptake. (C) Same as (B) but in live cells to allow uptake. In this case, after staining cell-surface bound anti-ICAM1 antibody counterparts with blue AlexaFluor350 secondary antibody, cells were permeabilized and stained with red AlexaFluor555 to access both surface and internalized anti-ICAM1. Thus, in (C) anti-ICAM1 colocalizing with cell-surface NCs appears white (blue + red + green; open arrows) and anti-ICAM1 colocalizing with internalized NCs appears yellow (green + red = yellow, white arrowheads). (A-C) Scale bar = 10 µm. Dashed lines = cell borders viewed by bright field. (D) DLS measurements of the hydrodynamic diameter and PDI of non-coated polystyrene NCs, NCs coated with anti-ICAM1 added to the apical chamber above TNFα-treated HBMECs (AP input), the same NCs harvested from the basolateral chamber after 5 h incubation (BL output), or control cell medium (CM). Data expressed as mean ± SEM. *Coated NCs *vs.* non-coated NCs ($p<0.05$ by Student's t-test).

3.3. Altered NC transport across an NPD brain endothelial cell model. After these validations, NC transcytosis was studied. For this purpose, we used a 30 min binding pulse followed by removal of non-bound NCs from the apical chamber and the basolateral chamber, and subsequent incubation in NC-free medium, as in our previous studies [7, 11, 28]. This protocol ensures the removal of any possible leakage and allows us to trace transcytosis of NCs pre-bound to cells separately from the influence of binding, which was different for each NC as measured by radiotracing (Supplementary Figure S8), just as shown above for microscopy data (Figure 2). Both PLGA and polystyrene NCs showed similar transcytosis results, *i.e.* 44.5% and 41.4% of the cell bound fraction transcytosed to the basolateral chamber at 24 h (Supplementary Figure S9). Data indicated that basolateral transport of anti-TfR NCs decreased by ≈ 50-60% in the diseased model at all times tested, *i.e.* 3, 8 and 24 h (Figure 5A). Similarly, anti-GM1 NCs exhibited ≈ 77% decreased transport at respective times. In contrast, transport of anti-ICAM1 NCs increased in the disease model by 1.6-, 2-and 2.4- fold at 3, 8 and 24 h, respectively (Figure 5A). A similar trend was observed by examining the apparent permeability coefficient (Papp) over a 24 h period (Figure 5B). In addition, apical release of NCs pre-bound to cells was also observed (Figure 5C). This was lowered in diseased cells for NCs targeted to ICAM1. A lowering tendency was also observed for anti-TfR NCs, though this was not statistically significant. Hence, increased interaction with and transcytosis across NPD brain endothelial cell models, with decreased apical release observed for anti-ICAM1 NCs agreed with enhanced brain biodistribution observed in ASM KO mice (Figure 1C), and enhanced accumulation of anti-TfR NCs in NPD cell barrier models was likely due to decreased transcytosis across these cells without an increase in apical release, also in agreement with reduced brain accumulation in ASM KO mice. Decreased anti-GM1 NC transcytosis across this cell model did not result in enhanced accumulation in these cells, likely because a tendency to enhanced apical release was observed for the caveolar pathway (Figure 5C); yet, this could not explain the lack of changes seen in the brain of ASM KO mice (Figure 1C)

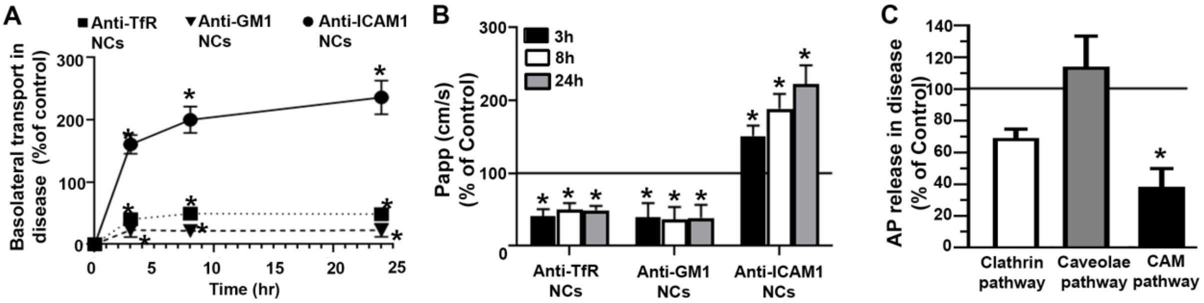

Figure 5: Transport of antibody coated NCs across control and NPD brain endothelial cell models. HBMECs were grown on transwells either untreated (Control) or treated with 20 μM imipramine + 10 ng/mL TNFα (Disease), following which they were incubated for a 30 min binding pulse with PLGA NCs coated with ^{125}I-anti-TfR, ^{125}I-anti-GM1 or ^{125}I-anti-ICAM1. Non-bound NCs were then removed from the apical and basolateral chambers and incubations continued in NC-free medium. (A) Basolateral fractions were collected at 3, 8 and 24 h to determine the number of NCs using a gamma counter and corrected for free iodine arising by degradation and was expressed for diseased cells as % of the control cells. (B) Apparent permeability coefficient (Papp) calculated from the same data using the formula described in Materials and Methods. (C) The apical fraction of NCs targeted to each of the pathways was also collected at 2 h and quantified. Data expressed as mean ± SEM. *Comparison with control cells ($p<0.05$ by Student's t-test).

3.4. Altered expression of markers associated with transcytosis in NPD cell models and brain samples of LSD patients. To shed some light on the discrepant results found for anti-GM1 NCs, we examined the expression of respective cell-surface elements to which each of the NCs was targeted, *i.e.* ganglioside GM1, TfR, and ICAM1. Flow cytometry to detect cell-surface expression indicated that GM1 surface levels were increased by 12-fold in the NPD model compared to control HMBECs, TfR surface levels were decreased by 40%, and ICAM1 surface levels were increased by 300-fold (Figure 6). A tendency to increased ICAM1 and GM1 levels observed by Western blot and immunostaining (Supplementary Figures S10 and S11) validated these results via independent methods. However, this was not the case for TfR, whose total expression obtained by Western blot was not reduced (Supplementary Figure S12) compared to surface expression reduction observed by flow cytometry (Figure 6). Thus, data on ICAM-1 expression were in accord with enhanced interaction and transcytosis of anti-ICAM1 NCs, in cell models and brain accumulation in mice. Results on TfR surface expression correlate with reduced transcytosis of anti-TfR NCs across cells and brain accumulation *in vivo*. However, data on GM1 levels were conflicting with those seen for anti-GM1 NCs.

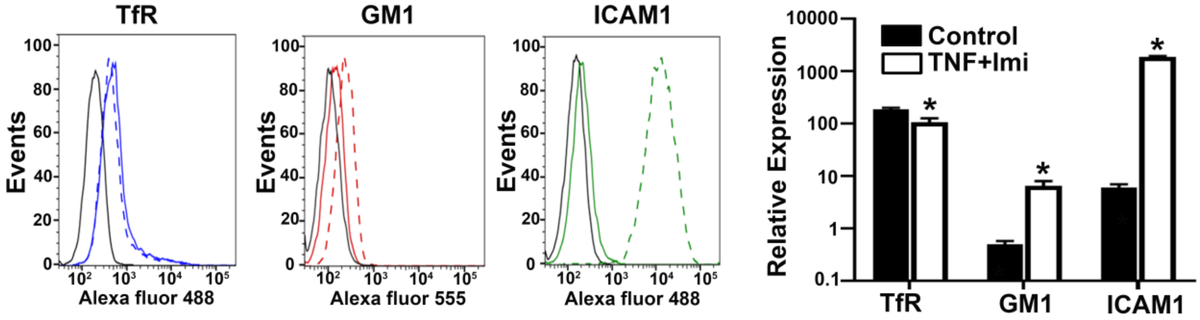

Figure 6: Levels of cell-surface markers to which NCs were targeted. Flow cytometry analysis of cell-surface markers to which NCs had been targeted *i.e.* TfR, ganglioside GM1, and ICAM1 in HBMECs, either untreated (Control) or treated with 20 μM imipramine + 10 ng/ml TNFα (disease) to mimic NPD. Solid black line = non-specific IgG. Solid colored lines = specific antibodies under control condition. Dashed colored lines = specific antibodies under disease condition. Quantification was done using FlowJo® software and expressed taking into consideration both intensity levels and positive fraction of the cell population, as described in Materials and Methods. Data expressed as mean ± SEM. *Compared to control ($p<0.05$ by Student's t-test).

To further investigate the discrepancy concerning GM1 results, we examined the levels of caveolin-1 (Cav-1) as this may relate to caveolar-mediated transport of anti-GM1 NCs. For instance, transport of caveolar-targeted cargo has been shown to be inhibited in Cav-1 deficient models [40]**.** Western blot analysis on cell lysates revealed that the expression of this marker was reduced by 60% in the NPD brain endothelial cell model compared to control cells (Figure 7). Additionally, Cav-1 was decreased to not detectable levels in brain samples from a NPD Type C patient, also called NPC (Supplementary Figure S13), which was historically co-classified with ASM deficient NPD since it associates with secondary sphingomyelin storage [41]. Western blot analysis also demonstrated, though not statistically significant, a tendency toward decreased expression of clathrin heavy chain levels (CHC; Figure 7), an intracellular marker involved in clathrin-mediated transport [42] associated to TfR, for which this results pairs well with decreased performance associated with respective NCs. Similarly, there was a slight, but not statistically significant, decrease in the expression of NHE-1, a transmembrane sodium/proton exchanger that interacts with ICAM-1 and is involved in CAM-mediated endocytosis [43, 44].

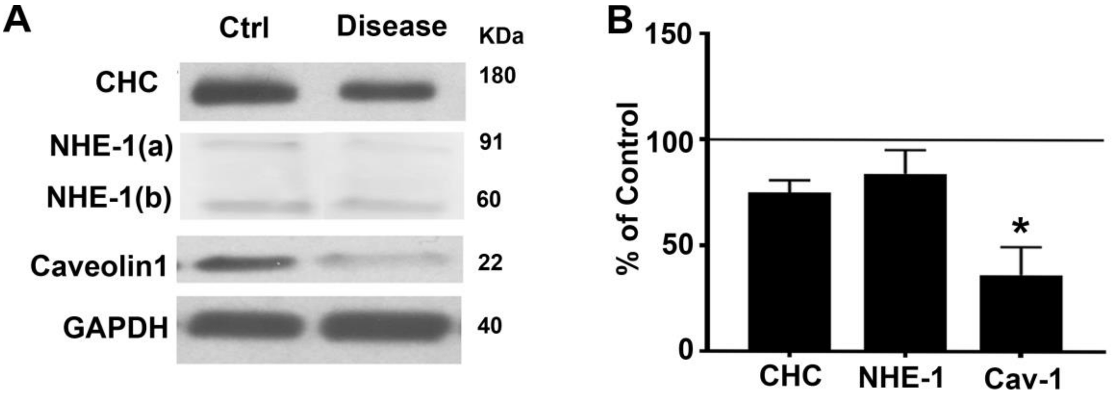

Figure 7: Expression of regulatory markers of endocytosis in NPD cell models. (A) Representative Western blots of NHE-1 involved in the ICAM-1-mediated transport, clathrin heavy chain (CHC) involved in TfR-mediated transport, caveolin-1 (Cav-1) associated with caveolae, and housekeeping GAPDH in untreated HBMEC (control,

Ctrl) or HBMEC treated with imipramine to mimic NPD (Disease). (B) Densitometric quantification of bands shown in (A) using ImageJ and normalized to respective housekeeping bands. The solid line indicates control condition. Data expressed as mean ± SEM. *Compared to control ($p<0.05$ by Student's t-test).

Finally, given the parallels found between Cav-1 levels in cellular models and human brain samples (Figure 7 and supplementary Figure S13), we examined whether the alterations previously observed in cellular and mouse models would correlate with clinical specimens (Supplementary Table S1). Human brain samples were first analyzed by immunohistochemistry (Figure 8A, Supplementary Figure S14) to determine the levels of CHC (associated with clathrin-mediated transport [42,45] as for TfR), Cav-1 (associated with caveolar-mediated transport [45] as for GM1), and ICAM-1 (associated with CAM-mediated transport [46]). Fluorescence microscopy observation showed decreased CHC and Cav-1 levels across ten different brain samples from patients of various LSDs regardless of sex, disease, and the age at disease onset, compared to three age-matching controls (Supplementary Figure S14). Further signal quantification corroborated that CHC and Cav-1 levels decreased by 70% and 60%, respectively, while ICAM-1 levels increased by 3.5-fold in the disease brains compared to control brains (Figure 8A). Furthermore, ICAM-1 levels were analyzed by Western blot in all the brains tested (Figure 8B) corroborating its increased expression in LSD *vs*. non-LSD brain samples, which was ≈ 2-fold when all samples were analyzed in bulk. Interestingly, this effect was more pronounced in samples from late-onset patients (3-fold increase) compared to early-onset patients (1.5-fold increase, not significant statistically).

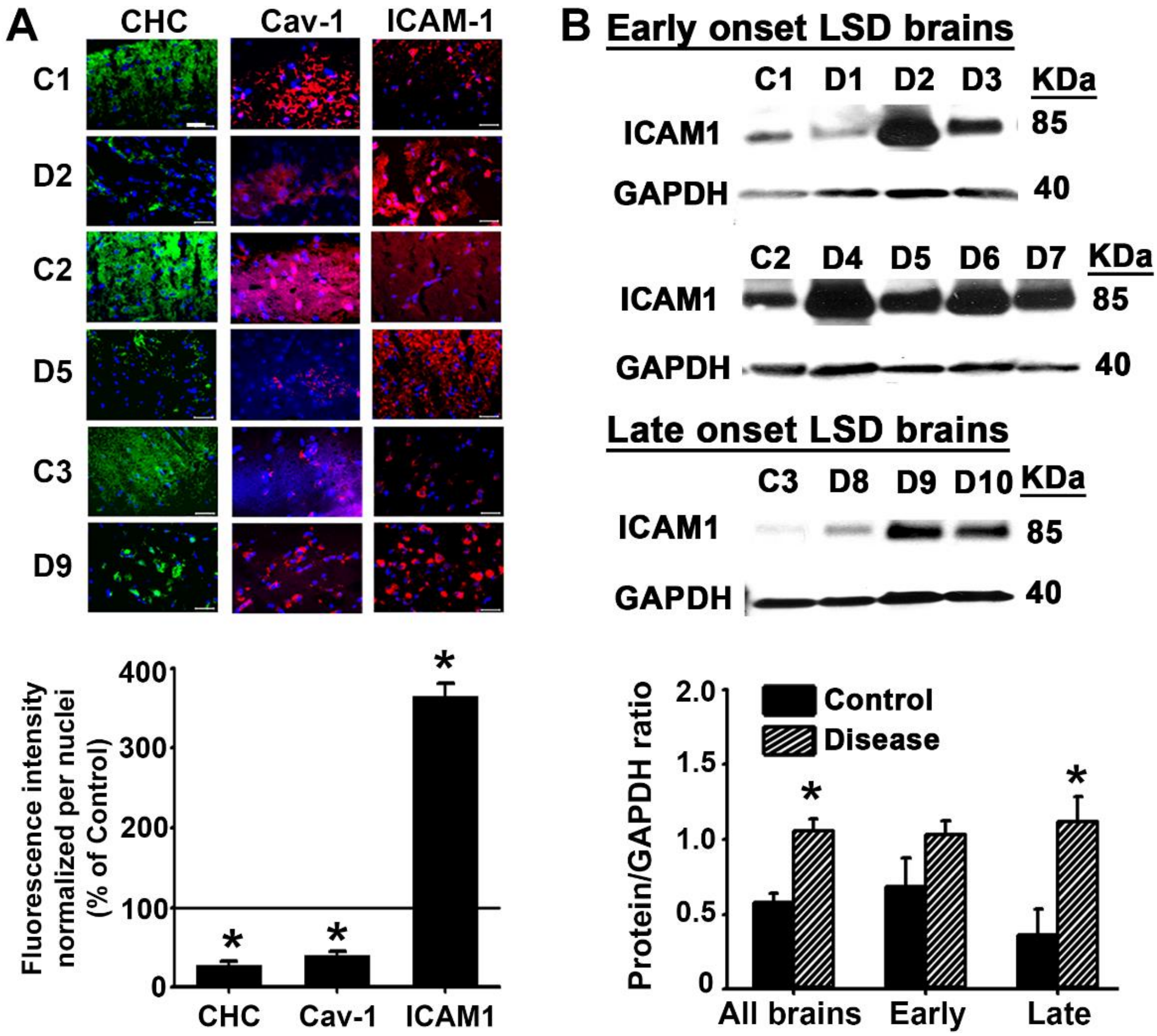

Figure 8: Expression of endocytic markers in human brains from LSD patients and non-LSD controls. (A) Representative immunohistochemistry images (top) and fluorescence intensity quantification (bottom) of brain samples from LSD patients (disease) *vs*. age-matched non-LSD controls, probed for clathrin heavy chain (CHC; green channel), caveolin-1 (Cav-1; red channel), and ICAM-1 (red channel). The signal of cell nuclei, visible in the blue channel, was used to normalize the fluorescence observed in the green and red channels, and the resulting expression levels in disease samples were expressed as % of expression in control samples. Scale bar = 40 µm. (B) Representative protein bands from Western blotting and densitometric quantification of human brain lysates probed for ICAM-1 and housekeeping protein GAPDH. (A, B) Samples are described in Supplementary Table S1 C= non-LSD control; D= LSD. Data expressed as mean ± SEM (n=6). *Compared to control ($p<0.05$ by one-way ANOVA, Holm-Sidak post hoc test).

4. Discussion

Numerous nanoformulations are being investigated to provide transport of therapeutics across the BBB by exploiting natural transcytosis pathways through brain endothelial cells [1-3]. However, it is becoming increasingly apparent that many diseases affecting the brain associate with abnormal storage of non-degraded macromolecules within cells, which often alters vesicular trafficking [12, 13, 15, 17-23]. This is the case for rare monogenic diseases such as LSDs [12, 13, 18-22] and common multifactorial conditions such as PD, AD, and cancers [15, 17, 23]. Whether these alterations affect transendothelial transport of therapeutic NCs remains largely unclear and was the core objective of this study. As a relevant example, we illustrated the value of these types of studies by focusing on ASM-deficient NPD, a LSD that affects both visceral organs and the CNS [3,27]. ERT for NPD is under clinical development [47], yet only for patients without the neurological component since recombinant ASM does not reach the brain from the circulation [37]. Hence, exploring the status of transcytosis routes in this disease shall best guide the development of alternative strategies to provide brain delivery, while also maintaining visceral delivery required for this disease. A summary of our findings is offered in Table 2, which will be further discussed below.

Table 2: Parameters affecting therapeutic delivery across the BBB in NPD models.

Parameter	**Clathrin**	**Caveolar**	**CAM**
Cell-surface level for the target receptor in brain endothelial cells	TfR ↓↓	GM1 ↑↑	ICAM-1 ↑↑↑↑
Endocytic marker expression in brain endothelial cells	CHC ↓	Cav-1 ↓↓	NHE-1 ↓
Receptor or endocytic marker expression in human brain samples *	CHC ↓	Cav-1 ↓↓↓	ICAM-1 ↑↑
NC interaction with cells (surface+intracellular)	↓↓	No change	↑↑↑
NC transcytosis across cells	↓↓	↓↓↓	↑↑
NC apical transport	↓	↑	↓↓
NC brain-specific accumulation in mice	↓	No change	↑↑

*The number of arrows is proportional to the reduction or increase observed. Black indicates statistical significance; grey indicates a visible change which is not statistically significant. *Brain samples did not encompass NPD but other neurological LSDs described in Table S1, with suspected trafficking alterations due to common traits, such as sphingomyelin storage.*

First, regarding a classical clathrin-associated route, the one mediated by TfR, we found decreased receptor expression at the plasmalemma in brain endothelial cells modeling NPD *vs*. controls (Figure 6). Similarly, CHC expression, a key component of clathrin coats on which TfR transport depends [42,48], showed a tendency to decrease in this cell model (not statistically significant; Figure 7) and was clearly reduced in brain samples from LSD patients (Figure 8A and Supplementary Figure S14). This correlates well with our previous observation showing decreased TfR-CHC colocalization in fibroblasts from NPD patients incubated with the TfR ligand, transferrin [19]. This may be caused by sequestration in endo-lysosomal vesicles and the trans-Golgi network where clathrin coats can form, since high sphingomyelin and cholesterol levels in NPD [27] impair membrane fusion involved in vesicular trafficking events [49]. As TfR requires CHC to traffic to and from the cell surface, the receptor may be intracellularly trapped due to CHC changes, preventing it from reaching or recycling to the cell surface. Indeed, supporting these observations, we found no change in the total TfR pool in NPD *vs*. control HBMECs (Supplementary Figure S12) and a tendency to decreased apical release of anti-TfR NCs interacting with brain endothelial monolayers (Figure 5C), with decreased basolateral transcytosis (Figure 5A), which would lead to increased cellular entrapment of these NCs, as manifested in Figure 2B. Such entrapment of anti-TfR in endolysosomal vesicles preventing their transcytosis have been seen in hCMEC endothelial cell barriers, especially under inhibition of endosomal acidification with bafilomycin [50]. Curiously, in one of our previous studies we found no differences in the cell-surface levels of transferrin upon incubation with fibroblasts from NPD patients *vs.* wildtype counterparts, from which we interpreted no changes in TfR cell-surface levels [19]. This discrepancy may be due to a different cell model being used and/or the fact that transferrin was simultaneously internalized into the cells, thus confounding the result, as we had acknowledged [19]. In contrast, in the present study we measured TfR expression on fixed cells, which more specifically reveals TfR steady state levels at the cell surface.

In accord with decreased TfR expression at the plasmalemma, we found decreased interaction of anti-TfR NCs with brain endothelial cells modeling NPD and grown on coverslips (Figure 2A). However, this was not the case when cells were grown on transwells, where an increase in NC interaction was observed (Figure 2B). And yet, despite this apparently increased NC interaction, transcytosis of anti-TfR NCs was decreased in NPD endothelial cell models grown on transwells (Figure 5), which correlates with decreased cell-surface expression of respective receptor and CHC. A logical explanation comes from the fact that endothelial cells acquire barrier phenotype as demonstrated here (Figure 3) and, thus, transcytosis functions only in a scenario where apical and basolateral surfaces separate [50, 51]. Therefore, reduced NC transcytosis to the basolateral side in the transwell model would render more NCs trapped on and/or within barrier cells, giving the impression of increased NC interaction, which could not be seen in a coverslip model where transcytosis is not possible. Correlating with this set of results, specific brain accumulation of anti-TfR NCs, best represented by brain SI-to-liver SI (Figure 1C) was also decreased in ASM KO mice compared to wildtype controls.

Second, with regards to targeting the caveolar pathway, anti-GM1 NCs were used. Unlike TfR, GM1 levels increased in brain endothelial cells modeling NPD (Figure 6) and mouse brains (Supplementary Figure S11), as it has been previously seen for gangliosides in several LSDs, including NPD and NPC [25]. This is because the primary lipid accumulation, such as sphingomyelin in NPD [27], often alters intertwined cellular metabolic routes resulting in secondary lipid storage [16, 25, 27]. Additionally, sphingomyelin and gangliosides interact in lipid-raft domains of the plasmalemma and, particularly, the neck of caveolae [52, 53]. Hence, aberrant sphingomyelin accumulation in NPD is expected to also sequester gangliosides at these sites [27, 52, 53]. Because of this disturbance and because cholesterol, which also accumulates secondarily in NPD [27], affects the oligomerization of caveolins at the plasmalemma [54], malfunction of caveolar-mediated pathways would be expected in this disease. We speculate that these phenomena contributed to the observed tendency of increased apical release of NCs targeting this route and decreased transcytosis of anti-GM1 NCs across brain endothelial cells modeling NPD (Figure 5). Reduced Cav-1 levels found in disease cell models and brain samples from an NPC patient (Figure 7, Supplementary Figure S13) may have also contributed to this result, since NPC is characterized by similar accumulation of these lipid-raft components [25, 41, 54]. Lower Cav-1 levels could be explained by the fact that cholesterol regulates transcription of Cav-1 gene through sterol-regulatory element binding proteins (SREBPs), whereby high cholesterol levels downregulate the expression of this gene [55].

A contrasting result regarding anti-GM1 NCs is that their interaction with brain endothelial cells mimicking NPD did not change compared to controls (Figure 2), despite GM1 levels being increased. It is possible that disturbance of lipid-raft domains and caveolae due to increased sphingomyelin, cholesterol and ganglioside levels in this disease may disrupt the normal display of GM1 [53] and, thus, its accessibility to NCs [56]. Increased apical release of

NCs interacting with diseased cells (Figure 5C), because of detachment or recycling, may also have contributed to the apparent lack of increase of NC-cell interaction despite the increased GM1 levels found. Alternatively, NCs may already be interacting with control cells at or close to saturation levels and, thus, any additional enhancement in GM1 levels would not result in enhanced NC targeting. This type of phenomenon has been documented [56, 57], including the case of ICAM-1 where inflammatory stimulation increases ICAM-1 expression by orders of magnitude while it only increases anti-ICAM1 NC targeting a few fold [35]. In fact, the same outcome was observed in this study where disease increased ICAM-1 expression by 300-fold in endothelial cells (Figure 6) and 3.5-fold in human brain samples that contain additional cell types (Figure 8), enhancing NC interaction with cells by 5- to 20-fold (Figure 2). Finally, brain-specific levels of anti-GM1 NC did not vary for ASM KO mice compared to wildtype (Figure 1). This may be due to the fact that decreased transcytosis across endothelial cells may be compensated by increased GM1 levels observed in mouse brains (Supplementary Figure S11), which would provide a means for a more sustained brain uptake. This compensation is possible *in vivo* but not in the cellular model used, because the binding-pulse + transport-chase protocol employed in cell culture does not provide a sustained supply of NCs, contrary to the *in vivo* situation where targeting and transcytosis occur concomitantly. Alternatively, anti-GM1 NCs may utilize compensatory mechanisms other than the caveolar pathway, since a reduced caveolae presence has been observed in the brain endothelium [58]. It must also be noted that quantification of the *in vivo* data yields the total counts in the particular organ without discriminating between each of its sub-compartments. A lack of change *in vivo* can simply mean that the anti-GM1 NCs are bound to the endothelial cells to a similar extent in disease *vs*. control, however, in the absence of effective endocytosis and transcytosis mechanisms, possibly correlating with reduced Cav-1 expression, this may not translate to effective NC transcytosis, as we observed (Figure 5).

Third, regarding anti-ICAM1 NCs, all parameters tested showed enhancement in cellular, animal, and human samples of NPD. This includes enhanced: ICAM-1 expression in brain endothelial cells modeling NPD and brain samples from LSD patients (Figures 6 and 8), NC interaction with cell models (Figure 2, Supplementary Figures S6, S8), transcytosis (Figure 5), and brain accumulation in mice (Figure 1). ICAM-1 overexpression by inflammatory factors subjacent to most pathologies is well documented and has been observed for NPD and other LSDs [59-62]. As discussed above, ICAM-1 expression increased by a much higher factor than NCs targeting, presumably due to steric hindrances limiting the number of NCs that can be bound to the cell surface [57], as observed in our previous studies [35]. Despite this, the increase in cellular interaction of anti-ICAM1 NCs was very significant (5 to 20-fold), the highest observed among the targets examined (Figure 2). This result, along with reduced apical release of cell-interacting NCs observed (Figure 5C) may have rendered the enhanced transcytosis found for this formulation. ASM deficiency is known to lower CAM endocytosis rate as this enzyme contributes to the signaling regulating this pathway [43, 63]. The expression of the CAM-endocytosis associated marker NHE-1 was slightly, yet not statistically, reduced in NPD models (Figure 7). This suggests a possible effect on this endocytic pathway as well. In fact, a closer observation of this study reveals that the increase in transcytosis was not as high as that of ICAM-1 expression or NC interaction, indirectly pointing to potential transcytosis alterations (Table 2). However, as for GM1 above, it has been shown that ICAM-1 overexpression compensates for this reduced rate, enhancing absolute transport [61]. Additionally, previous data have shown that ICAM-1 recycles to the cell surface replenishing the pool of receptors that can engage in transport [61]. Altogether, these facts explain enhanced anti-ICAM1 NCs transcytosis in NPD models and correlates well with increased brain-specific accumulation of this formulation in ASM KO mice.

To our best knowledge, this is the first time that endocytic markers have been examined in human brain samples from multiple LSDs (Figure 8; Supplementary Figure S14). Importantly, results derived from these clinical specimens revealed common alterations that are in agreement with our cellular and *in vivo* data, which should be borne in mind while designing therapeutics for LSDs and, by extension, other disorders that exhibit lysosomal dysfunction and/or aberrant accumulation of macromolecular species. For instance, reductions in Cav-1 expression have been correlated with AD neuropathology [64]. TfR can increase or decrease in different pathological states [4]. In a study evaluating the clathrin pathway in AD, no changes were seen in TfR expression or uptake by endothelial cells [65]. However, that study used a monomolecular anti-TfR antibody, which may render different results than multimolecular anti-TfR NCs. In fact, literature shows that compared to low affinity anti-TfR antibodies, high affinity counterparts trigger lysosomal trafficking of the antibody-receptor complex in brain endothelial cells with TfR degradation, which leads to decreased TfR levels [66-68], similar to our observations. Since NCs bear multiples copies of an antibody and their affinities are much higher than free antibodies [35], it is possible that anti-TfR NCs could exacerbate this response, resulting in lower TfR surface expression (further hindered by inadequate recycling of TfRs to the cell surface) and transcytosis, as we observed. The targeting valency (number of antibody molecules) of anti-ICAM1 NCs has also been shown to play a key role in transcytosis, whereby slow binding at the endothelial apical surface limits the efficacy of low targeting valency NCs, slow detachment from the endothelial basolateral surface limits the efficacy of high targeting valency NCs, while NCs displaying an intermediate targeting valency perform best because they are less limited regarding these two steps [11]. Similar results have been shown for other receptors and pathways, such as those involving the formation of tubular structures for mid-avidity NCs targeted to LRP1 [69] or monovalent anti-TfR antibodies [70]. Different intravascular administration routes can greatly impact these outcomes even when the same formulation is used. For instance, anti-ICAM1 liposomes injected *i.v.* showed 10-fold higher uptake in the inflamed brain *vs*. control brain [71]. When injected via the carotid artery, an additional 5-fold elevation was observed due to absence of a lung-first pass effect [71]. Speculatively, immune cell-based therapies may show benefit as a drug delivery carrier for LSDs since they rely on the expression of inflammatory markers to extravasate across the BBB [72], similar to the anti-ICAM1 NCs.

These data also highlight the different and complementary results obtained through use of different model systems regarding the study of NC interactions by cells and transport across a barrier-like cellular monolayer. For instance, endothelial cells adopt a polarized phenotype when grown on a transwell, and exhibit differences in the processing of endocytosed cargo as seen for anti-TfR NCs (Figure 2). Such polarized model systems are of value in prescreening formulations prior to *in vivo* studies; yet, investigating parameters such as binding independently of transport can also increase our mechanistic understanding of drug delivery processes. It was by comparing both models that we could discern that anti-TfR NCs were getting entrapped in cell-barrier models of disease, providing the appearance of enhanced interaction yet leading to lower transcytosis. We also found a good *in vitro*-to-*in vivo* correlation between the NPD transwell model and ASM KO mice *vs*. respective controls, for both anti-TfR NCs and anti-ICAM1 NCs (Figure 1, 5). For instance, anti-TfR NCs exhibited a ~50% reduction in transport in the transwell model and ~50% reduction in brain accumulation *in vivo*. Anti-ICAM1 NCs exhibited ~3-fold increase in cellular transport as well as brain accumulation *in vivo* in the disease models. A priori, the transwell model did not efficiently predict the outcomes for anti-GM1 NCs *in vivo*: 77 % transport reduction in NPD-cell model but no change *in vivo* in the ASM KO model. However, a more detailed study revealed the role of the enhanced GM1 expression found *in vivo* as a possible explanation for this fact.

Altogether, these studies highlight the importance of testing multiple models and assay types in early stages of NC development to best understand their behavior. These data also reveal the diversity of outcomes depending on the specific endothelial receptor targeted, the precise pathology under investigation, the particular properties of the drug delivery system used, the model systems used for testing, and the administration route, but also the fact that through these studies we are beginning to extract commonalities that shall guide our design of therapeutic interventions.

5. Conclusions

Using several models of NPD and other LSDs, this study demonstrates various alterations of molecular elements associated with brain transcytosis pathways, which lead to changes in the transendothelial transport of NCs targeted to these routes. In disease models, reduced cell-surface levels of TfR, reduced expression of CHC, and reduced cellular transcytosis and mouse brain accumulation of anti-TfR NCs were found. Also, reduced Cav-1 expression, increased apical release of cell-interacting NCs, and reduced transcytosis of anti-GM1 NCs were observed, yet increased GM1 levels seemed to compensate, providing similar brain accumulation of this formulation in disease *vs*. control mice. Increased ICAM-1 expression, reduced apical release of cell-interacting NCs, and increased transcytosis and brain distribution of anti-ICAM1 NCs were found in disease. Therefore, identifying possible alterations in these transport mechanisms is key to select the best routes for therapeutic targeting and help design effective NC for this purpose.

Supplementary Materials:

Table S1. Human brain samples used in this study.

Table S2: Biodistribution of anti-ICAM1 NCs in wildtype mice.

Figure S1. Biodistribution of ^{125}I-IgG tracer injected free *vs*. non-targeted NCs or targeted NCs.

Figure S2. *In vivo* biodistribution of targeted NCs in wildtype mice.

Figure S3. Specific binding of polystyrene NCs to brain endothelial cell models.

Figure S4. Specific uptake of targeted polystyrene NCs in brain endothelial cell models.

Figure S5. Sphingomyelin levels in a pharmacological model of NPD brain endothelial cells.

Figure S6. Targeting of polystyrene and PLGA NCs to brain endothelial cell barrier models.

Figure S7. Specificity of transport of antibody coated NCs across a brain endothelial barrier model.

Figure S8. Cell binding of targeted NCs to a control v/s NPD brain endothelial barrier model.

Figure S9. Transport of polystyrene and PLGA NCs across an NPD brain endothelial cell barrier model.

Figure S10. ICAM1 expression in NPD cell models by Western blot.

Figure S11. Histochemistry of cholera toxin subunit B in mouse brains.

Figure S12: Transferrin receptor expression in cell models.

Figure S13: Caveolin-1 expression in human brain samples.

Figure S14. Immunohistology of endocytic markers in human brains from LSD patients and non-LSD controls.

Author Contributions: Conceptualization, M.S. and S.M.; Experimentation, M.S., M.L., R.M., R.B., M. V., M.A.; writing—original draft preparation, M.S.; writing—review and editing, M.S., S.M.; supervision, S.M.; funding acquisition, M.S., S.M. All authors have read and agreed to the published version of the manuscript.

Funding: This research was funded by the Lysosomal Disease Network (U54NS065768), a part of the NCATS Rare Diseases Clinical Research Network (RDCRN), an initiative of the Office of Rare Diseases Research (ORDR), funded through a collaboration between NCATS and the National Institute of Neurological Disorders and Stroke (NINDS), and the National Institute of Diabetes and Digestive and Kidney Diseases (NIDDK) (M.S.). Funding also came from National Institutes of Health project R01 HL98416, the Spanish Ministry of Science and Innovation project RTI2018–101034-B-I00 (MICIE/FEDER), and the CERCA Program (Generalitat de Catalunya) (S.M.). Additional funding includes the InPhiNIT Predoctoral Fellowship program (LCF/BQ/DI18/11660018) from Fundación La Caixa and Horizon 2020 Marie Sklodowska-Curie (grant 713673) (M.L.).

Acknowledgments: Authors thank Vignesh Pernati, Ella Atsavapranee and Jordi Long for technical help with some analysis and organization.

Conflicts of Interest: The authors declare no conflict of interest.

References

1. Abdul Razzak, R.; Florence, G. J.; Gunn-Moore, F. J., Approaches to CNS drug delivery with a focus on transporter-mediated transcytosis. *International journal of molecular sciences* **2019,** *20* (12), 3108.
2. Saraiva, C.; Praça, C.; Ferreira, R.; Santos, T.; Ferreira, L.; Bernardino, L., Nanoparticle-mediated brain drug delivery: Overcoming blood–brain barrier to treat neurodegenerative diseases. *Journal of Controlled Release* **2016,** *235*, 34-47.
3. Muro, S., Strategies for delivery of therapeutics into the central nervous system for treatment of lysosomal storage disorders.*Drug Deliv. Transl. Res.* **2012**, *2*, 169-186.
4. Johnsen, K. B.; Burkhart, A.; Thomsen, L. B.; Andresen, T. L.; Moos, T., Targeting the transferrin receptor for brain drug delivery. *Progress in Neurobiology* **2019,** *181*, 101665.
5. Sorets, A. G.; Rosch, J. C.; Duvall, C. L.; Lippmann, E. S., Caveolae-mediated transport at the injured blood–brain barrier as an underexplored pathway for central nervous system drug delivery. *Current Opinion in Chemical Engineering* **2020,** *30*, 86-95.
6. Boado, R. J.; Lu, J. Z.; Hui E. KW.; Lin, H.; Pardridge, W. M., Bi-functional IgG-lysosomal enzyme fusion proteins for brain drug delivery. *Sci Rep* **2019,** *9*, 18632.

7. Hsu, J.; Rappaport, J.; Muro, S., Specific binding, uptake, and transport of ICAM-1-targeted nanocarriers across endothelial and subendothelial cell components of the blood-brain barrier. *Pharmaceutical Research* **2014,** *31* (7), 1855-1866.
8. Del Grosso, A., Galliani, M., Angella, L., Santi, M., Tonazzini, I., Parlanti, G., Signore, G., & Cecchini, M. Brain-targeted enzyme-loaded nanoparticles: A breach through the blood-brain barrier for enzyme replacement therapy in Krabbe disease. *Science advances* **2019**, *5*(11), eaax7462.
9. Johnsen, K. B.; Bak, M.; Kempen, P. J.; Melander, F.; Burkhart, A.; Thomsen, M. S.; Nielsen, M. S.; Moos, T.; Andresen, T. L., Antibody affinity and valency impact brain uptake of transferrin receptor-targeted gold nanoparticles. *Theranostics* **2018,** *8* (12), 3416-3436.
10. Park, T.E.; Singh, B; Li, H; Lee, J.Y.; Kang, S. K.; Choi, Y.J.; Cho, C.S., Enhanced BBB permeability of osmotically active poly(mannitol-co-PEI) modified with rabies virus glycoprotein via selective stimulation of caveolar endocytosis for RNAi therapeutics in Alzheimer's disease. *Biomaterials* **2015**, *38*, 61-71.
11. Manthe, R. L.; Loeck, M.; Bhowmick, T.; Solomon, M.; Muro, S., Intertwined mechanisms define transport of anti-ICAM nanocarriers across the endothelium and brain delivery of a therapeutic enzyme. *J Control Release* **2020,** *324*, 181-193.
12. Gabandé-Rodríguez, E., Pérez-Cañamás, A., Soto-Huelin, B., Mitroi, D. N., Sánchez-Redondo, S., Martínez-Sáez, E., Venero, C., Peinado, H., & Ledesma, M. D. Lipid-induced lysosomal damage after demyelination corrupts microglia protective function in lysosomal storage disorders. *The EMBO journal* **2019**, *38*(2), e99553.
13. Fukuda, T.; Ewan, L.; Bauer, M.; Mattaliano, R. J.; Zaal, K.; Ralston, E.; Plotz, P. H.; Raben, N., Dysfunction of endocytic and autophagic pathways in a lysosomal storage disease. *Ann Neurol* **2006,** *59* (4), 700-708.
14. Sweeney, M. D.; Sagare, A. P.; Zlokovic, B. V., Blood-brain barrier breakdown in Alzheimer disease and other neurodegenerative disorders. *Nat Rev Neurol* **2018,** *14* (3), 133-150.
15. Abeliovich, A.; Gitler, A. D., Defects in trafficking bridge Parkinson's disease pathology and genetics. *Nature* **2016,** *539* (7628), 207-216.
16. Ballabio, A.; Gieselmann, V., Lysosomal disorders: from storage to cellular damage. *Biochimica et biophysica acta* **2009,** *1793* (4), 684-696.
17. Muro, S., Alterations in cellular processes involving vesicular trafficking and implications in drug delivery. *Biomimetics (Basel)* **2018,** *3* (3), 19.
18. Teixeira, C. A.; Miranda, C. O.; Sousa, V. F.; Santos, T. E.; Malheiro, A. R.; Solomon, M.; Maegawa, G. H.; Brites, P.; Sousa, M. M., Early axonal loss accompanied by impaired endocytosis, abnormal axonal transport, and decreased microtubule stability occur in the model of Krabbe's disease. *Neurobiol Dis* **2014,** *66*, 92-103.
19. Rappaport, J.; Garnacho, C.; Muro, S., Clathrin-mediated endocytosis is impaired in type A-B Niemann-Pick disease model cells and can be restored by ICAM-1-mediated enzyme replacement. *Mol Pharm* **2014,** *11* (8), 2887-2895.
20. Rappaport, J.; Manthe, R. L.; Solomon, M.; Garnacho, C.; Muro, S., A comparative study on the alterations of endocytic pathways in multiple lysosomal storage disorders. *Mol Pharm* **2016**, *13* (2), 357-368

21. Simons, K.; Gruenberg, J., Jamming the endosomal system: lipid rafts and lysosomal storage diseases. *Trends in cell biology* **2000,** *10* (11), 459-462.
22. Tecedor, L.; Stein, C. S.; Schultz, M. L.; Farwanah, H.; Sandhoff, K.; Davidson, B. L., CLN3 loss disturbs membrane microdomain properties and protein transport in brain endothelial cells. *J Neurosci* **2013,** *33* (46), 18065-79.
23. Mellman I, Yarden Y. Endocytosis and cancer. *Cold Spring Harb Perspect Biol* **2013**, *5* (12), a016949.
24. Kaur, G.; Lakkaraju, A., Early Endosome morphology in health and disease. *Advances in experimental medicine and biology* **2018,** *1074*, 335-343.
25. Breiden, B.; Sandhoff, K., Mechanism of secondary ganglioside and lipid accumulation in lysosomal disease. *International journal of molecular sciences* **2020,** *21* (7), 2566.
26. Shahmoradian, S. H.; Lewis, A. J.; Genoud, C.; Hench, J.; Moors, T. E.; Navarro, P. P.; Castaño-Díez, D.; Schweighauser, G.; Graff-Meyer, A.; Goldie, K. N.; Sütterlin, R.; Huisman, E.; Ingrassia, A.; Gier, Y. d.; Rozemuller, A. J. M.; Wang, J.; Paepe, A. D.; Erny, J.; Staempfli, A.; Hoernschemeyer, J.; Großerüschkamp, F.; Niedieker, D.; El-Mashtoly, S. F.; Quadri, M.; Van Ijcken, W. F. J.; Bonifati, V.; Gerwert, K.; Bohrmann, B.; Frank, S.; Britschgi, M.; Stahlberg, H.; Van de Berg, W. D. J.; Lauer, M. E., Lewy pathology in Parkinson's disease consists of crowded organelles and lipid membranes. *Nature Neuroscience* **2019,** *22* (7), 1099-1109.
27. Schuchman, E. H., The pathogenesis and treatment of acid sphingomyelinase-deficient Niemann-Pick disease. *J Inherit Metab Dis.* **2007**, *30* (5), 654-663.
28. Ghaffarian, R.; Bhowmick, T.; Muro, S., Transport of nanocarriers across gastrointestinal epithelial cells by a new transcellular route induced by targeting ICAM-1. *J Control Release* **2012**, *163*(1), 25-33.
29. Roki, N.; Solomon, M.; Casta, L.; Bowers, J.; Getts, R.C.; Muro, S. A method to improve quantitative radiotracing-based analysis of the in vivo biodistribution of drug carriers. *Bioeng Transl Med*. **2021**; *6*:e10208.
30. Kim, J.; Sinha, S.; Solomon, M.; Perez-Herrero, E.; Hsu, J.; Tsinas, Z.; Muro, S., Co-coating of receptor-targeted drug nanocarriers with anti-phagocytic moieties enhances specific tissue uptake versus non-specific phagocytic clearance. *Biomaterials* **2017,** *147*, 14-25.
31. Garnacho, C.; Dhami, R.; Solomon M, Schuchman, E. H.; Muro, S., Enhanced delivery and effects of acid sphingomyelinase by ICAM-1-targeted nanocarriers in Type B Niemann-Pick disease mice. *Mol. Ther.* **2017**, *25* (7), 1686-1696.
32. Muntimadugu, E.; Silva-Abreu, M.; Vives, G.; Loeck, M.; Pham, V.; Del Moral, M.; Solomon, M.; & Muro, S. Comparison between Nanoparticle Encapsulation and Surface Loading for Lysosomal Enzyme Replacement Therapy. *International journal of molecular sciences* **2022**, *23*(7), 4034.
33. Wiseman, M. E.; Frank, C.W., Antibody adsorption and orientation on hydrophobic surfaces. *Langmuir* **2012**, *28* (3), 1765-1774.
34. Hsu, J.; Bhowmick, T.; Burks, S. R.; Kao J.P.; Muro, S., Enhancing biodistribution of therapeutic enzymes in vivo by modulating surface coating and concentration of ICAM-1-targeted nanocarriers. *J Biomed Nanotechnol*. **2014**, *10* (2), 345-354.

35. Muro, S.; Dziubla, T.; Qiu, W.; Leferovich, J.; Cui, X.; Berk, E.; Muzykantov, V. R., Endothelial targeting of high-affinity multivalent polymer nanocarriers directed to intercellular adhesion molecule 1. *J. Pharmacol. Exp. Ther.* **2006**, *317*, 1161-1169.
36. Hsu, J.; Serrano, D.; Bhowmick, T.; Kumar, K.; Shen, Y.; Kuo, Y. C.; Garnacho, C.; Muro, S., Enhanced endothelial delivery and biochemiocal effecs of a-galactosidase by ICAM-1 targeted nanocarriers for Fabry dieases. *J Control Release* **2011**, *149*(3), 323-331.
37. Miranda, S. R.; He, X.; Simonaro, C. M.; Gatt, S.; Dagan, A.; Desnick, R. J.; Schuchman, E. H., Infusion of recombinant human acid sphingomyelinase into niemann-pick disease mice leads to visceral, but not neurological, correction of the pathophysiology. *FASEB J.* **2000**, *14* (13), 1988-95.
38. Dodge, J. C.; Clarke, J.; Treleaven, C. M.; Taksir, T. V.; Griffiths, D. A.; Yang, W.; Fidler, J. A.; Passini, M. A.; Karey, K. P.; Schuchman, E. H.; Cheng, S. H.; Shihabuddin, L. S., Intracerebroventricular infusion of acid sphingomyelinase corrects CNS manifestations in a mouse model of Niemann-Pick A disease. *Experimental Neurology* **2009,** *215* (2), 349-357.
39. Beckmann, N.; Sharma, D.; Gulbins, E.; Becker, K. A.; Edelmann, B., Inhibition of acid sphingomyelinase by tricyclic antidepressants and analogons. *Frontiers in physiology* **2014,** *5*, 331.
40. Razani, B.; Engelman, J. A.; Wang, X. B.; Schubert, W.; Zhang, X. L.; Marks, C. B.; Macaluso, F.; Russell, R. G.; Li, M.; Pestell, R. G.; Di Vizio, D.; Hou, H. Jr; Kneitz, B.; Lagaud, G.; Christ, G. J.; Edelmann, W.; Lisanti, M. P., Caveolin-1 null mice are viable, but show evidence of hyper-proliferative and vascular abnormalities. *J Biol Chem.* **2001**, *276*, 38121–38138.
41. Newton, J.; Milstien, S.; Spiegel, S., Niemann-Pick type C disease: The atypical sphingolipidosis. *Advances in biological regulation* **2018**, *70*, 82–88.
42. Doxsey, S. J.; Brodsky, F. M;, Blank, G. S.; Helenius, A., Inhibition of endocytosis by anti-clathrin antibodies. *Cell* **1987**, *50* (3), 453–463.
43. Serrano, D.; Bhowmick, T.; Chadha, R.; Garnacho, C.; Muro, S., Intercellular adhesion molecule 1 engagement modulates sphingomyelinase and ceramide, supporting uptake of drug carriers by the vascular endothelium. *Arteriosclerosis, thrombosis, and vascular biology* **2012**, *32*(5), 1178–1185.
44. Muro, S.; Mateescu, M.; Gajewski, C.; Robinson, M;, Muzykantov, V. R;, Koval, M. Control of intracellular trafficking of ICAM-1-targeted nanocarriers by endothelial Na+/H+ exchanger proteins. *American journal of physiology. Lung cellular and molecular physiology* **2006**, *290*(5), L809–L817.
45. Doherty, G. J.; McMahon, H. T., Mechanisms of endocytosis. *Annual review of biochemistry* **2009**, *78*, 857–902.
46. Muro, S.; Wiewrodt, R.; Thomas, A.; Koniaris, L.; Albelda, S. M.; Muzykantov, V. R.; Koval, M., A novel endocytic pathway induced by clustering endothelial ICAM-1 or PECAM-1. *Journal of cell science* **2003**, *116* (8), 1599–1609.
47. Wasserstein, M. P.; Jones, S. A.; Soran, H.; Diaz, G. A.; Lippa, N.; Thurberg, B. L.; Culm-Merdek, K.; Shamiyeh, E.; Inguilizian, H.; Cox, G. F.; Puga, A. C., Successful within-patient dose escalation of olipudase alfa in acid sphingomyelinase deficiency. *Molecular genetics and metabolism* **2015**, *116* (1-2), 88–97.

48. Qian, Z. M.; Li, H.; Sun, H.; Ho, K., Targeted drug delivery via the transferrin receptor-mediated endocytosis pathway. *Pharmacological reviews* **2002**, *54* (4), 561–587.
49. Traub, L. M.; Bannykh, S. I.; Rodel, J. E.; Aridor, M.; Balch, W. E.; Kornfeld, S., AP-2-containing clathrin coats assemble on mature lysosomes. *The Journal of cell biology* **1996**, *135* (6), 1801–1814
50. Sade, H.; Baumgartner, C.; Hugenmatter, A.; Moessner, E.; Freskgård, P.-O.; Niewoehner, J., A human blood-brain barrier transcytosis assay reveals antibody transcytosis influenced by pH-dependent receptor binding. *PLOS ONE* **2014,** *9* (4), e96340.
51. Banks W. A., Blood–brain barrier as a regulatory interface. *Forum Nutr*. **2009**, *63*, 102–10.
52. Posse de Chaves, E.; Sipione, S., Sphingolipids and gangliosides of the nervous system in membrane function and dysfunction. *FEBS letters* **2010,** *584* (9), 1748–1759.
53. Sonnino, S.; Prinetti, A., Sphingolipids and membrane environments for caveolin. *FEBS letters* **2009**, *583* (4), 597–606.
54. Gévry, N.; Schoonjans, K.; Guay, F.; Murphy, B. D., Cholesterol supply and SREBPs modulate transcription of the Niemann-Pick C-1 gene in steroidogenic tissues. *Journal of lipid research* **2008**, *49* (5), 1024–1033.
55. Bist, A.; Fielding, P. E.; Fielding, C. J., Two sterol regulatory element-like sequences mediate up-regulation of caveolin gene transcription in response to low density lipoprotein free cholesterol. *Proceedings of the National Academy of Sciences* **1997**, *94* (20), 10693–10698.
56. Hoshyar, N.; Gray, S.; Han, H.; Bao, G., The effect of nanoparticle size on in vivo pharmacokinetics and cellular interaction. *Nanomedicine (London, England)* **2016**, *11* (6), 673–692.
57. Rhoden, J. J.; Dyas, G. L.; Wroblewski, V. J., A Modeling and experimental investigation of the effects of antigen density, binding affinity, and antigen expression ratio on bispecific antibody binding to cell surface targets. *The Journal of biological chemistry* **2016**, *291* (21), 11337–11347.
58. Tuma, P.; Hubbard, A. L., Transcytosis: Crossing cellular barriers. *Physiological Reviews* **2003,** *83* (3), 871-932.
59. Muro, S., Intercellular adhesion molecule-1 and vascular cell adhesion molecule-1. In: Aird W, ed. *Endothelial biomedicine.* Cambridge University Press, New York, NY **2007**, 1058-1070.
60. Sumagin, R.; Sarelius, I. H., TNF-α activation of arterioles and venules alters distribution and levels of ICAM-1 and affects leukocyte-endothelial cell interactions. *American Journal of Physiology-Heart and Circulatory Physiology* **2006,** *291* (5), H2116-H2125.
61. Muro, S.; Schuchman, E. H.; Muzykantov, V. R., Lysosomal enzyme delivery by ICAM-1-targeted nanocarriers bypassing glycosylation- and clathrin-dependent endocytosis. *Molecular therapy* **2006,** *13* (1), 135–141.
62. Bosch, M. E.; Kielian, T., Neuroinflammatory paradigms in lysosomal storage diseases. *Frontiers in neuroscience* **2015,** *9*, 417.
63. Manthe, R. L.; Rappaport, J. A.; Long, Y.; Solomon, M.; Veluvolu, V.; Hildreth, M.; Gugutkov, D.; Marugan, J.; Zheng, W.; Muro, S., δ-Tocopherol effect on endocytosis and its combination with enzyme replacement therapy for lysosomal disorders: A New Type of Drug Interaction?. *The Journal of pharmacology and experimental therapeutics* **2019**, *370*(3), 823–833.
64. Bonds, J. A.; Shetti, A.; Bheri, A.; Chen, Z.; Disouky, A.; Tai, L.; Mao, M.; Head, B. P.; Bonini, M. G.; Haus, J. M.; Minshall, R. D.; Lazarov, O., Depletion of caveolin-1 in type 2 diabetes model

induces alzheimer's disease pathology precursors. *The Journal of Neuroscience* **2019,** *39* (43), 8576-8583.

65. Bourassa, P.; Alata, W.; Tremblay, C.; Paris-Robidas, S.; Calon, F., Transferrin receptor-mediated uptake at the blood–brain barrier is not impaired by alzheimer's disease neuropathology. *Molecular Pharmaceutics* **2019,** *16* (2), 583-594.
66. Bien-Ly, N.; Yu, Y. J.; Bumbaca, D.; Elstrott, J.; Boswell, C. A.; Zhang, Y.; Luk, W.; Lu, Y.; Dennis, M. S.; Weimer, R. M.; Chung, I.; Watts, R. J., Transferrin receptor (TfR) trafficking determines brain uptake of TfR antibody affinity variants. *Journal of Experimental Medicine* **2014,** *211* (2), 233-244.
67. Yu, Y. J.; Zhang, Y.; Kenrick, M.; Hoyte, K.; Luk, W.; Lu, Y.; Atwal, J.; Elliott, J. M.; Prabhu, S.; Watts, R. J.; Dennis, M. S., Boosting brain uptake of a therapeutic antibody by reducing its affinity for a transcytosis target. *Science Translational Medicine* **2011,** *3* (84), 84ra44.
68. Haqqani, A. S.; Thom, G.; Burrell, M.; Delaney, C. E.; Brunette, E.; Baumann, E.; Sodja, C.; Jezierski, A.; Webster, C.; Stanimirovic, D. B., Intracellular sorting and transcytosis of the rat transferrin receptor antibody OX26 across the blood-brain barrier in vitro is dependent on its binding affinity. *Journal of neurochemistry* **2018**, *146* (6), 735–752.
69. Tian, X.; Leite, D. M.; Scarpa, E.; Nyberg, S.; Fullstone, G.; Forth, J.; Matias, D.; Apriceno, A.; Poma, A.; Duro-Castano, A.; Vuyyuru, M.; Harker-Kirschneck, L.; Šarić, A.; Zhang, Z.; Xiang, P.; Fang, B.; Tian, Y.; Luo, L.; Rizzello, L.; Battaglia, G., On the shuttling across the blood-brain barrier via tubule formation: Mechanism and cargo avidity bias. *Science Advances* **2020,** *6* (48), eabc4397.
70. Villasenor, R.; Schilling, M.; Sundaresan, J.; Lutz, Y.; Collin, L., Sorting tubules regulate blood-brain barrier transcytosis. *Cell Rep* **2017,** *21* (11), 3256-3270.
71. Marcos-Contreras, O. A.; Brenner, J. S.; Kiseleva, R. Y.; Zuluaga-Ramirez, V.; Greineder, C. F.; Villa, C. H.; Hood, E. D.; Myerson, J. W.; Muro, S.; Persidsky, Y.; Muzykantov, V. R., Combining vascular targeting and the local first pass provides 100-fold higher uptake of ICAM-1-targeted vs untargeted nanocarriers in the inflamed brain. *Journal of controlled release* **2019**, *301*, 54–61.
72. Vargason, A. M.; Anselmo, A. C.; Mitragotri, S., The evolution of commercial drug delivery technologies. *Nature biomedical engineering* **2021**, 10.1038/s41551-021-00698-w.

Supplementary Data

Altered blood-brain barrier transport of nanotherapeutics in lysosomal storage diseases

Melani Solomon [1*], Maximilian Loeck [2], Marcelle Silva-Abreau [2], Ronaldo Moscoso [1], Ronelle Bautista [1], Marco Vigo [2], and Silvia Muro [1,2,3*]

[1] Institute for Bioscience and Biotechnology Research, University of Maryland, College Park, MD, USA
[2] Institute for Bioengineering of Catalonia of the Barcelona Institute of Science and Technology, Barcelona, Spain
[3] Institute of Catalonia for Research and Advanced Studies, Barcelona, Spain

* Correspondence:
Nanocarrier targeting and transport: SM: muro@umd.edu; +34 934 020 440
Lysosomal storage disease markers: MS: melani.solomon@catalent.com

Keywords: Lysosomal storage disorders, neurological diseases, blood-brain barrier, transcytosis pathways, targeted nanocarriers.

Table S1. Human brain samples used in this study.

Sample	UMB ID	Age	Gender	Diagnosis
C1	1864	2y 178d	Female	Non-LSD
C2	1791	2y, 286d	Female	Non-LSD
C3*	5849	36y, 231d	Female	Non-LSD
D1	1768	Prenatal (16 wks gestation)	Male	Gaucher disease
D2	5100	294d	Male	Globoid cell leukodystrophy
D3	M3282M	95d	Male	Pompe disease
D4	5315	2y, 170d	Male	Tay-Sach's disease
D5	4770	2y, 343d	Female	Niemann-Pick disease Type C
D6	5596	1y, 247d	Female	GM1 gangliosidosis
D7	5745	3y, 215d	Female	Metachromatic Leukodystrophy
D8*	4299	50y, 349d	Male	Fabry disease
D9*	5010	22y, 64d	Male	Multiple sulfatase deficiency
D10*	1163	39y, 107d	Male	Globoid cell leukodystrophy

**Late onset; C=control; D=LSD; d=days; wks=weeks; y=years.*

Table S2: Biodistribution of anti-ICAM1 NCs in wildtype mice.

Bioistribution	**Anti ICAM/PS NCs** (Mean ± SEM)	**Anti-ICAM/PLGA NCs** (Mean ± SEM)
%ID in blood		
2 min	22.7 ± 2.8	16.5 ± 2.6
15 min	7.6 ± 0.9	8.9 ± 3.2
30 min	7.3 ± 0.5	7.6 ± 2.4
%ID/g organ (30 min)		
Blood	3.3 ± 0.43	4.4 ± 1.4
Brain	0.2 ± 0.02	0.2 ± 0.02
Heart	1.8 ± 0.2	1.4 ± 0.2
Kidneys	2.5 ± 0.2	4.0 ± 0.5
Liver	40.2 ± 9.2	34.3 ± 5.1
Lungs	104.2 ± 19.1	114.2 ± 27.9
Spleen	63.6 ± 11.3	34.8 ± 5.5

PLGA=poly(lactic-co-glycolic acid); PS=polystyrene. These formulations carried ½ targeting antibody compared to those shown in Figures S1, S2.

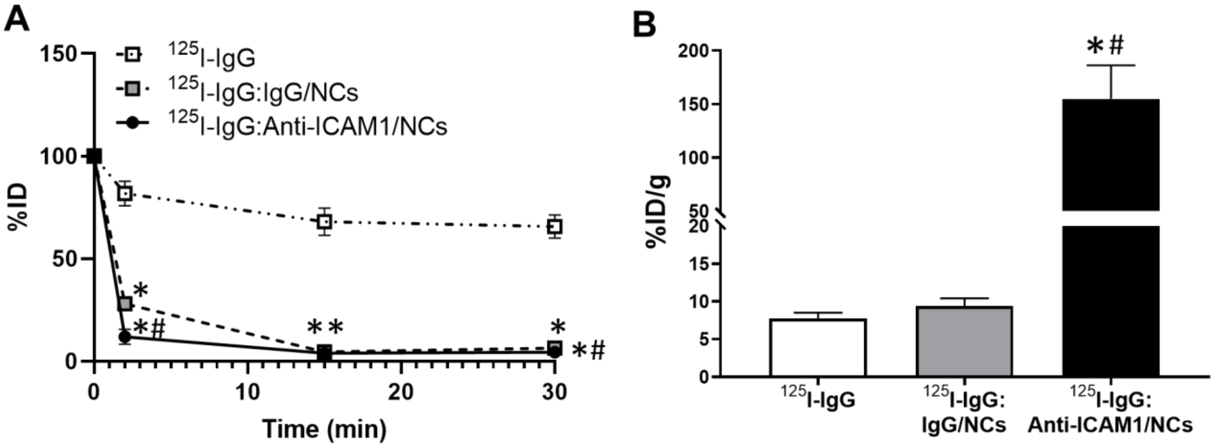

Figure S1. Biodistribution of ^{125}I-IgG tracer injected free *vs.* non-targeted NCs or targeted NCs. Wildtype mice were *i.v.* injected with model polystyrene NCs coated with anti-ICAM1 and tracer amounts of ^{125}I-IgG, NCs coated with IgG and tracer amounts of ^{125}I-IgG, or free ^{125}I-IgG. (A) Blood was collected at the indicated times and (B) lungs were obtained at sacrifice (30 min), weighed and measured in a gamma counter to calculate (A) the percentage of the injected dose (%ID) in the circulation and (B) the percentage of injected dose per gram of lung (%ID/g). Data are Mean ± SEM. *Each NC compared to free ^{125}I-IgG; #ICAM1 targeted NCs compared to non-targeted NCs ($p < 0.05$ by Student's t test).

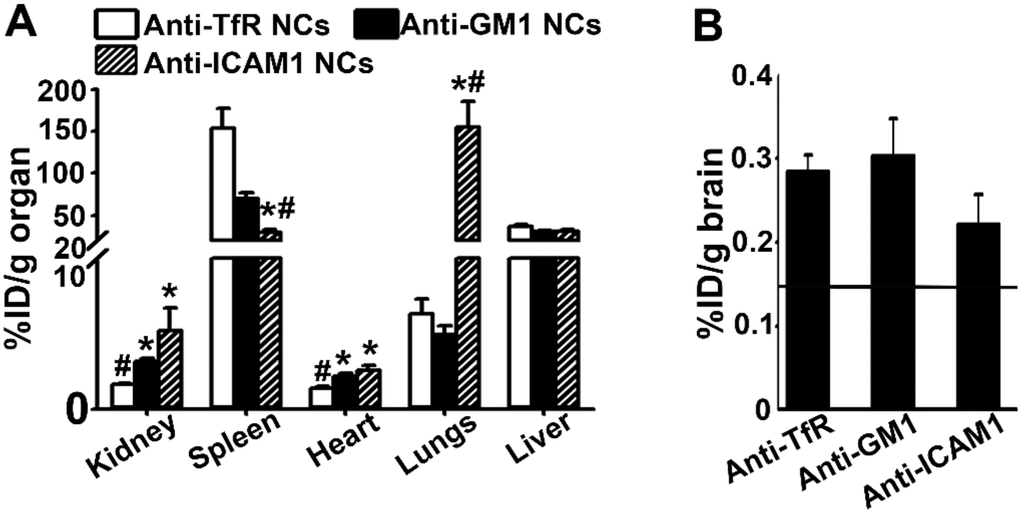

Figure S2. ***In vivo* biodistribution of targeted NCs in wildtype mice.** Wildtype mice were *i.v.* injected with model polystyrene NCs coated with tracer amounts of ^{125}I-IgG and either targeting anti-TfR, anti-GM1 or anti-ICAM1 or non-specific IgG control. Organs were collected at sacrifice (30 min) and their weight and ^{125}I content were determined to calculate (A) the percentage of injected dose in each visceral organ normalized by its weight (%ID/g) and (B) the percentage of injected dose in brain normalized by its weight (%ID/g). The solid line indicates IgG NCs. Data are Mean ± SEM. *Compared to anti-TfR NCs, #compared to anti-GM1 NCs ($p < 0.05$ by Student's t test).

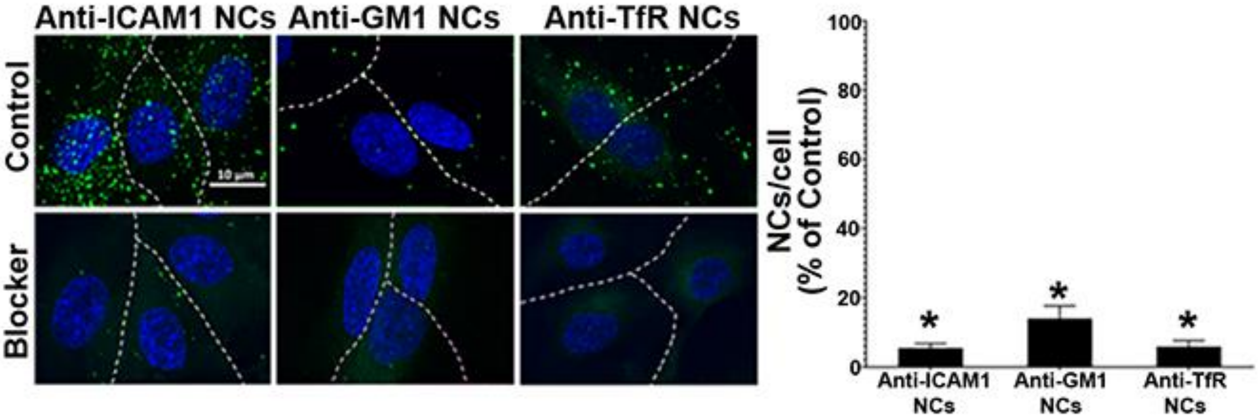

Figure S3. Specific binding of polystyrene NCs to brain endothelial cell models. Immunofluorescence micrographs (left) and quantification (right), showing interaction of FITC-labeled polystyrene NCs coated with anti-TfR, anti-GM1 or anti-ICAM1 with HBMECs after 1 h incubation at 37 °C in the presence of control medium or medium containing respective blockers (anti-ICAM1, anti-GM1, or anti-TfR). Dashed lines = cell borders viewed by bright field. Blue = nuclei stained with DAPI. Scale bar = 10 μm. Data expressed as mean ± SEM. *Comparison to control cells ($p<0.05$ by Student's t-test).

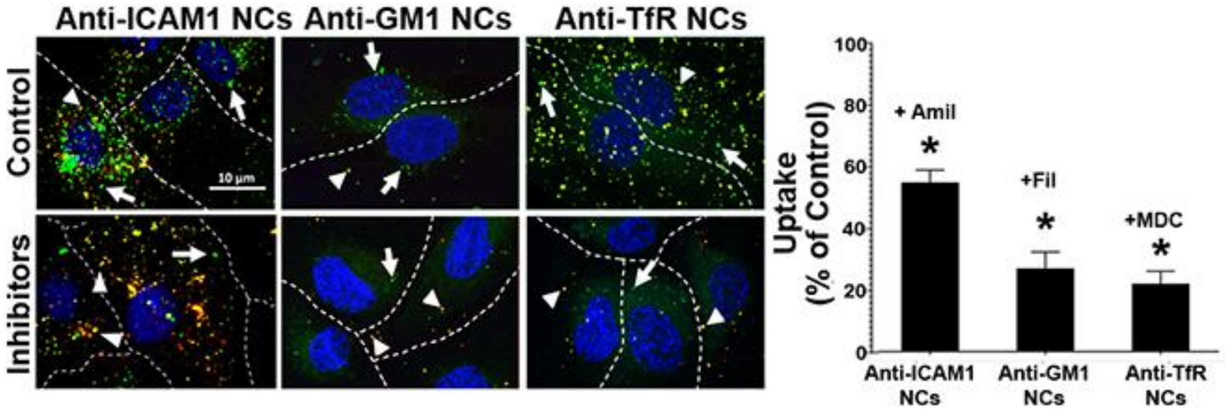

Figure S4. Specific uptake of targeted polystyrene NCs in brain endothelial cell models. Immunofluorescence micrographs (left) and quantification (right), showing interaction of FITC-labeled polystyrene NCs coated with anti-TfR, anti-GM1 or anti-ICAM1 with HBMECs after 1 h incubation at 37 °C in the presence of control medium or medium containing amiloride (Amil) to inhibit CAM-mediated endocytosis, Filipin (Fil) to inhibit caveolae-mediated endocytosis, or monodansylcadaverine (MDC) to inhibit clathrin-mediated endocytosis. Cells were washed and fixed, then incubated with AlexaFluor555-conjugated secondary antibody to counterstain cell-surface NCs in red and distinguish them (red+green=yellow: arrowheads) from internalized NCs (green alone: arrows). Dashed line = cell borders viewed by bright field. Blue = nuclei stained with DAPI. Scale bar = 10 µm. Data expressed as mean ± SEM. *Comparison with control cells ($p<0.05$ by Student's t-test).

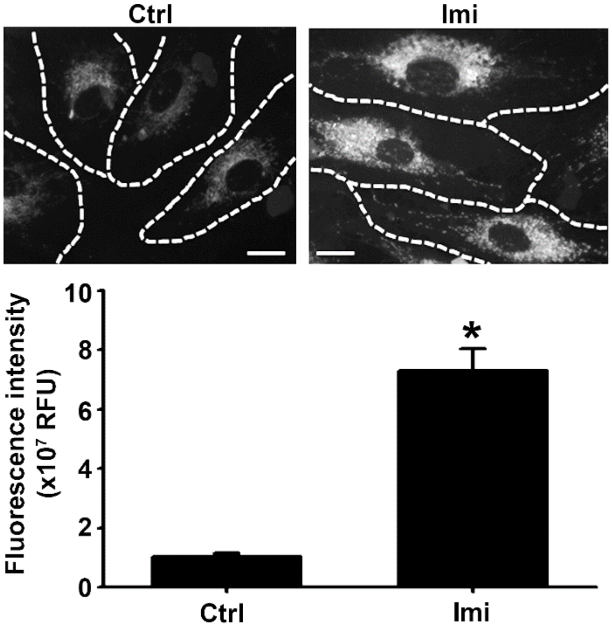

Figure S5. Sphingomyelin levels in a pharmacological model of NPD brain endothelial cells. HBMECs were left untreated (Ctrl) or treated for 48 h with 20 µM imipramine (Imi) to pharmacologically induce ASM deficiency. (Upper panel) Representative fluorescence microscopy images of cells incubated for 24 h with fluorecent BODIPY-F12 sphingomyelin, an ASM substrate, followed by fixation and mounting for fluorescence microscopy. Scale bar = 10 µm. (Lower panel) Quantification of fluorescence intensity of the BODIPY label. Data are Mean ± SEM. *Comparison to control HBMECs ($p < 0.05$ by Student's t test).

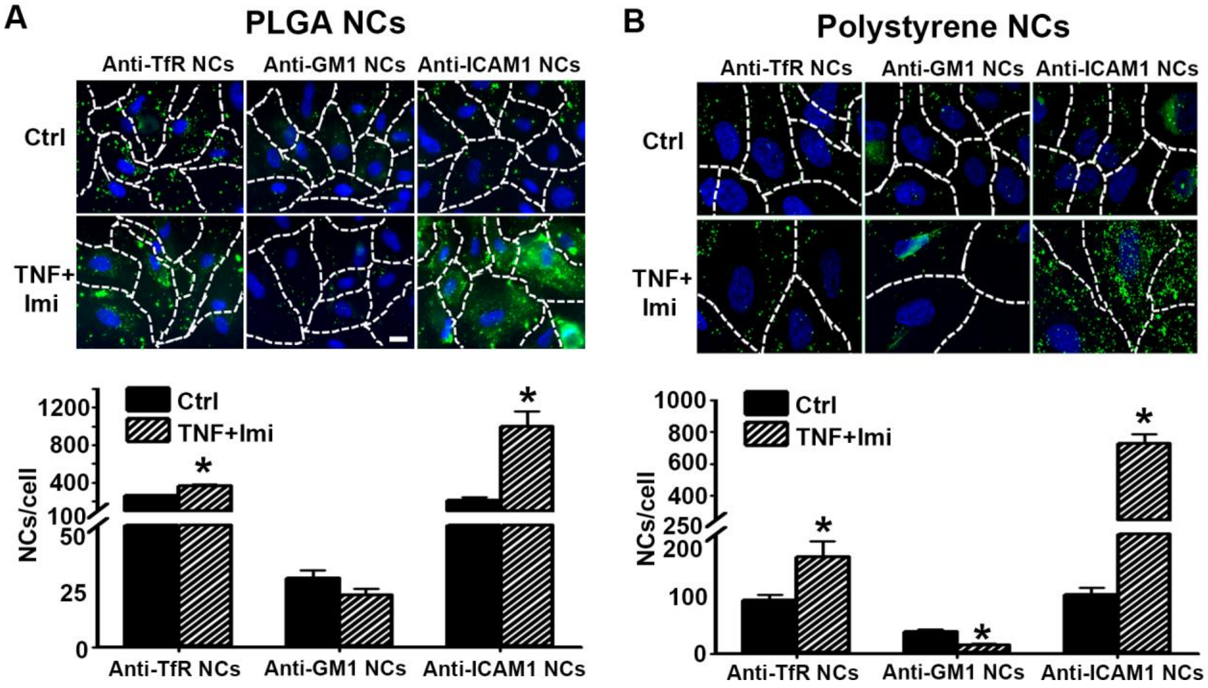

Figure S6. Targeting of polystyrene and PLGA NCs to brain endothelial cell barrier models. Immunofluorescence micrographs (top panels) and quantification (bottom panels), showing interaction of (A) PLGA *vs.* (B) FITC-labeled polystyrene NCs coated with anti-TfR, anti-GM1 or anti-ICAM1 with HBMECs grown on transwells either untreated (Ctrl) or treated to mimic a disease condition (TNF+Imi). Incubations were conducted for 30 min at 37 °C, after which cells were (A) fixed, permeabilized, and incubated with respective FITC-labeled secondary antibodies (green) to detect antibody-coated NCs and DAPI (blue) to stain cell nuclei, or (B) fixed and incubated with DAPI (blue) to stain nuclei, Scale bar = 10 μm. Data expressed as mean ± SEM. *Comparison with control cells ($p<0.05$ by Student's t-test).

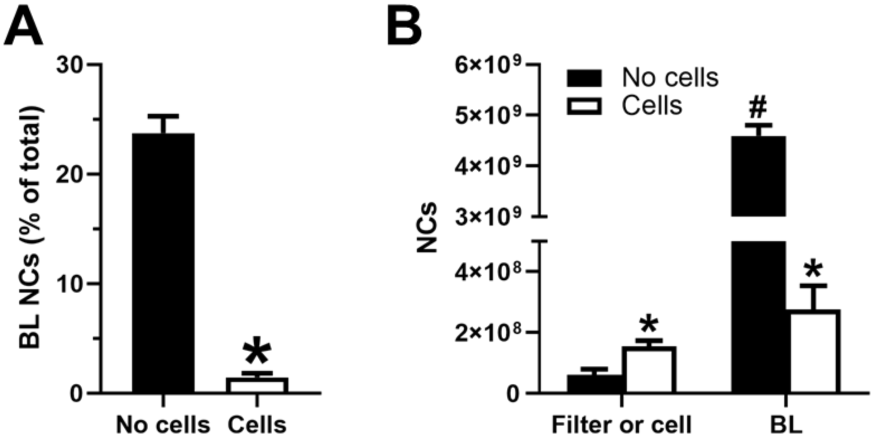

Figure S7. Specificity of transport of antibody coated NCs across a brain endothelial barrier model. Transwell filters, containing or not an HBMEC monolayer, were incubated for 30 min at 37 °C with ^{125}I-labeled anti-ICAM1 polystyrene NCs added to the apical chamber, after which ^{125}I content was determined in all three fractions: apical (AP), cell-covered filter or pristine filter, and basolateral (BL). Data expressed as mean ± SEM (n=4). *Cell *vs.* no cell comparison; #BL vs. filter or cell ($p<0.05$ by Student's t-test).

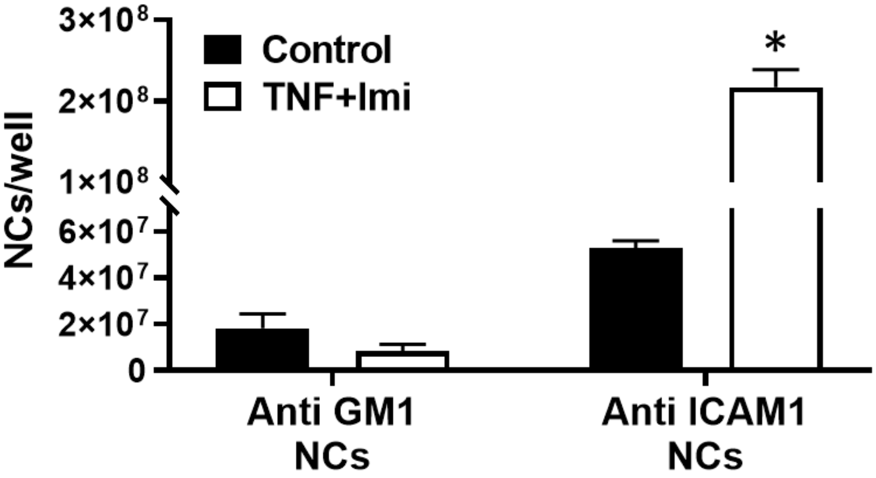

Figure S8. Cell binding of targeted NCs to a control *vs.* NPD brain endothelial barrier model. HBMECs grown on transwell filters were incubated for 30 min at 37 °C with ^{125}I-labeled anti-GM1 or anti-ICAM1 PLGA NCs added to the apical chamber, after which cell fractions were collected and their ^{125}I contents were determined and corrected for degradation to calculate the number of NCs in the cell fraction. Data expressed as mean ± SEM. *Comparison to control condition ($p<0.05$ by Student's t-test).

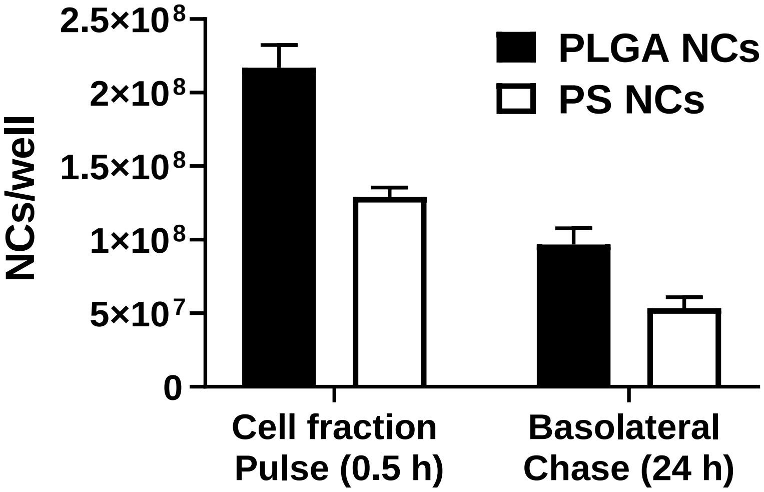

Figure S9. Transport of polystyrene and PLGA NCs across an NPD brain endothelial barrier model. TNFα-treated HBMECs grown on transwell filters were incubated for 30 min at 37 °C with ^{125}I-labeled anti-ICAM1 polystyrene or PLGA NCs added to the apical chamber, after which both the apical and basolateral chambers were washed, and cell fractions collected for half the wells to determine the cell fraction at pulse. Post washing, incubations were continued in NC-free cell medium for 24 h. Following this chase period, the basolateral cell media were collected and their ^{125}I content determined to calculate the number of NCs in basolateral fraction at chase. Data expressed as mean ± SEM. The NCs transported to the basolateral chamber from the cell-bound fraction were similar for both NCs ($p>0.05$).

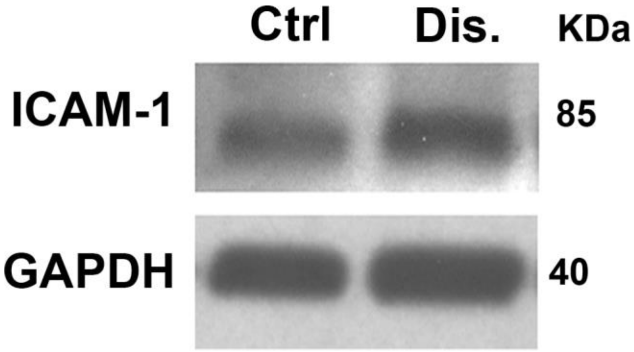

Figure S10. ICAM-1 expression in NPD cell models by Western blot. Representative Western blots to detect ICAM-1 and housekeeping GAPDH protein levels in HBMEC lysates either untreated (Ctrl) or treated with imipramine (Dis.) to mimic NPD.

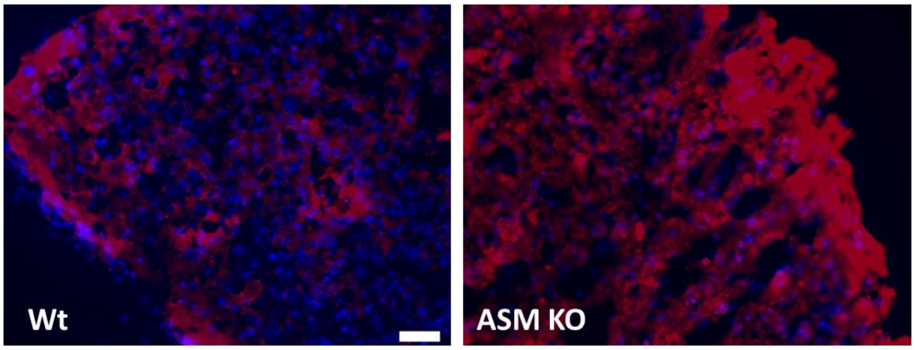

Figure S11. Histochemistry of cholera toxin subunit B in mouse brains. Representative micrographs of brain sections from wildtype (Wt) *vs*. ASM KO mice incubated with AlexaFluor594-conjugated cholera toxin subunit B (CTB; red) to stain ganglioside GM1 and DAPI to stain cell nuclei (blue). Scale bar = 50 μm.

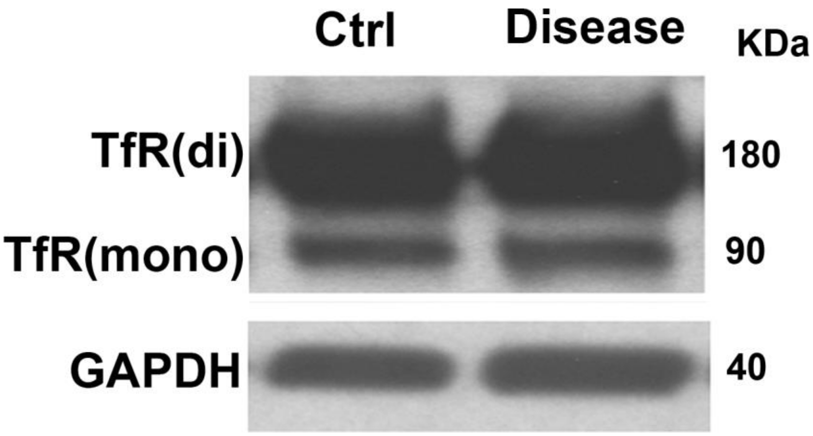

Figure S12: Transferrin receptor expression in cell models. Representative Western blots to detect transferrin receptor (TfR) and housekeeping GAPDH protein levels in HBMEC lysates either untreated (Ctrl) or treated with imipramine (Disease) to mimic NPD. Mono= monomer of TfR, di = Dimer of TfR.

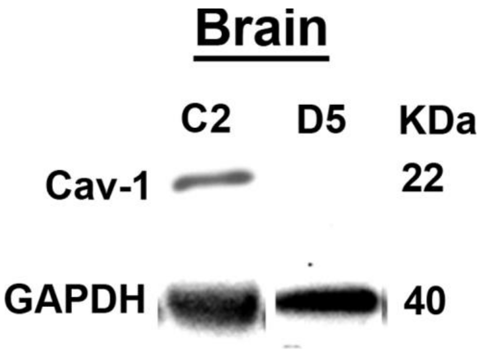

Figure S13: Caveolin-1 expression in human brain samples. Representative Western blots to detect caveolin-1 (Cav-1) and housekeeping GAPDH protein levels in a brain sample from a Niemann Pick Type C patient (D5) compared to an age-matched non-LSD control (C2).

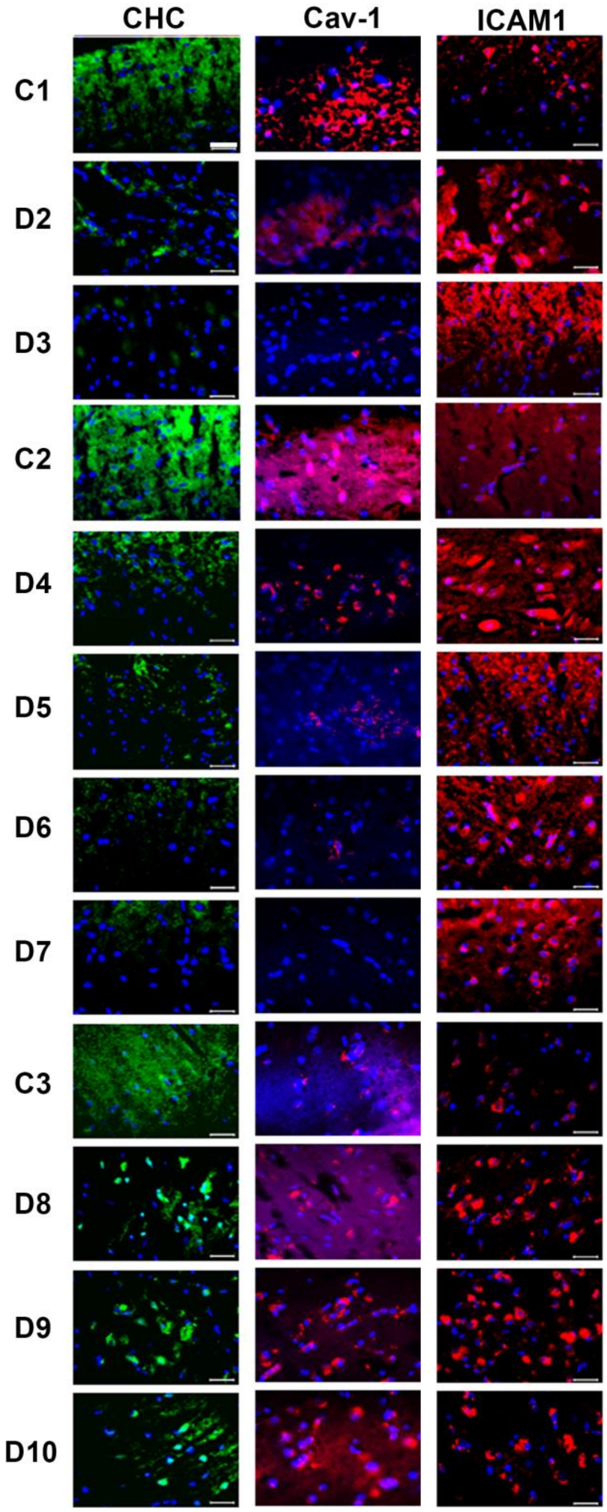

Figure S14. Immunohistology of endocytic markers in human brains from LSD patients and non-LSD controls. Representative images of brain sections from LSD patients (D) vs. age-matched non-LSD controls (C), probed for clathrin heavy chain (CHC; green channel), caveolin-1 (Cav-1; red channel) and ICAM1 (red channel). Cell nuclei are visible in the blue channel. Scale bar = 40 μm. Samples are described in supplemental Table S1.